

How Baryonic Processes affect Strong Lensing properties of Simulated Galaxy Clusters

M. Killedar^{1,2*}, S. Borgani^{1,2,3}, M. Meneghetti^{4,5}, K. Dolag^{6,7}, D. Fabjan^{1,8,9}
& L. Tornatore¹

¹ *Dipartimento di Fisica dell'Università di Trieste, Sezione di Astronomia, Via Tiepolo 11, I-34131 Trieste, Italy*

² *INAF - Osservatorio Astronomico di Trieste, Via G.B. Tiepolo 11, I-34131 Trieste, Italy*

³ *INFN - National Institute for Nuclear Physics, Via Valerio 2, I-34127 Trieste, Italy*

⁴ *INAF - Osservatorio Astronomico di Bologna, Via Ranzani 1, I-40127 Bologna, Italy*

⁵ *INFN - Sezione di Bologna, Viale Berti Pichat 6/2, I-40127 Bologna, Italy*

⁶ *Universitätssternwarte München, München, Germany*

⁷ *Max-Planck-Institut für Astrophysik, Garching, Germany*

⁸ *SPACE-SI, Slovenian Centre of Excellence for Space Sciences and Technologies, Aškerčeva 12, 1000 Ljubljana, Slovenia*

⁹ *Faculty of Mathematics and Physics, University of Ljubljana, Jadranska 19, 1000 Ljubljana, Slovenia*

Accepted 2012 August 23. Received 2012 August 23; in original form 2012 August 03

ABSTRACT

The observed abundance of giant arcs produced by galaxy cluster lenses and the measured Einstein radii have presented a source of tension for Λ CDM, particularly at low redshifts ($z \sim 0.2$). Previous cosmological tests for high-redshift clusters ($z > 0.5$) have suffered from small number statistics in the simulated sample and the implementation of baryonic physics is likely to affect the outcome. We analyse zoomed-in simulations of a fairly large sample of cluster-sized objects, with $M_{\text{vir}} > 3 \times 10^{14} h^{-1} M_{\odot}$, identified at $z = 0.25$ and $z = 0.5$, for a concordance Λ CDM cosmology. These simulations have been carried out by incrementally increasing the physics considered. We start with dark matter only simulations, and then add gas hydrodynamics, with different treatments of baryonic processes: nonradiative cooling, radiative cooling with star formation and galactic winds powered by supernova explosions, and finally including the effect of AGN feedback. Our analysis of strong lensing properties is based on the computation of the cross-section for the formation of giant arcs and of the Einstein radii. We find that the addition of gas in non-radiative simulations does not change the strong lensing predictions significantly, but gas cooling and star formation together significantly increase the number of expected giant arcs and the Einstein radii, particularly for lower redshift clusters *and* lower source redshifts. Further inclusion of AGN feedback reduces the predicted strong lensing efficiencies such that the lensing probability distributions becomes closer to those obtained for simulations including only dark matter. Our results indicate that the inclusion of baryonic physics in simulations will not solve the arc-statistics problem at low redshifts, when the physical processes included provide a realistic description of cooling in the central regions of galaxy clusters. As outcomes of our analysis, we encourage the adoption of Einstein radii as a robust measure of strong lensing efficiency, and provide the Λ CDM predictions to be used for future comparisons with high-redshift cluster samples.

Key words: gravitational lensing: strong – galaxies: clusters – methods: N-body simulations – cosmology: theory

1 INTRODUCTION

The hierarchical formation paradigm describes a scenario in which small structures form earlier and then merge to

* E-mail: killedar@oats.inaf.it (MK)

form more massive objects. This description within the Λ CDM model has been highly successful at explaining observations of structure on a large range of scales and redshifts (e.g. Efstathiou et al. 1990; White & Frenk 1991; Komatsu et al. 2011), including the formation of galaxy clusters (e.g. Kravtsov & Borgani 2012). However, the internal structure of galaxy clusters has posed a challenge. The earliest comparisons between simulated clusters and the observed frequency of gravitational lensing arcs revealed a serious discrepancy between the observations and Λ CDM predictions (Bartelmann et al. 1998; Li et al. 2005). More recent comparisons to X-ray selected clusters find that the discrepancy remains for $z < 0.3$ and $z > 0.5$ but results are not definitive due to small simulated sample sizes at higher redshifts and uncertainties with selection procedures and biases (Meneghetti et al. 2011; Horesh et al. 2011). In addition, observations of clusters at redshifts $0.1 < z < 0.6$ have found higher concentrations and larger Einstein radii than predicted (Broadhurst & Barkana 2008; Sadeh & Rephaeli 2008; Zitrin et al. 2011). These are related problems since both suggest a failure of Λ CDM to correctly infer the distribution of matter in the cores of clusters; the solution may be found in the details of the simulations used to formulate the predictions.

Simulations which only incorporate collisionless particles are commonplace in the literature. Dark matter structure is evolved under gravity with the effect of baryons ignored. On large-scales, the distribution of gas follows the dark matter potential wells, so the collisionless simulations will suffice; however on galaxy- and group- scales, gas cooling, star formation and feedback can alter the gravitational potential significantly (e.g. Blumenthal et al. 1986; Gnedin et al. 2004). Early simulations that were used to model the cluster lenses did not incorporate sufficient relevant physical processes (Hattori et al. 1997; Sadeh & Rephaeli 2008). These simulations were originally justified by the premise that the temperature of the ICM is too hot to allow efficient cooling, so the baryonic matter must simply follow the dark matter potential and would not have a significant impact on its shape (e.g. Broadhurst & Barkana 2008). The role of baryons in shaping galaxy clusters has recently become a key point of discussion since hydrodynamic simulations have become more feasible; the findings are that baryons do, in fact, affect the shapes of gravitational potential of the simulated haloes. Gas cooling, for example, leads to adiabatic compression of galaxy haloes preferentially in the cluster centre, allowing more mass to be deposited around the core (Barkana & Loeb 2010). Cooling and star formation serve to steepen the density profile of clusters and thus increase the mass concentration and the strong lensing cross-section (Lewis et al. 2000; Gnedin et al. 2004; Puchwein et al. 2005; Rozo et al. 2008; Rudd et al. 2008; Cui et al. 2012). Unfortunately, these processes lead to the well known overcooling problem, in which the cold gas mass and stellar mass in the cluster core is overestimated.

Including in simulations feedback from gas accretion onto supermassive black holes (SMBHs) is a promising solution for overcooling (Sijacki et al. 2007; Teyssier et al. 2011; McCarthy et al. 2010; Fabjan et al. 2010), while simultaneously reproducing the drop in the cosmic SFR for $z < 2$ (e.g., van de Voort et al. 2011). The resulting feedback from active galactic nuclei (AGN) significantly reduces the gas

fraction in simulated galaxy-groups and poor clusters ($T \lesssim 2\text{keV}$), but cannot remove gas from the deep potential wells of rich, massive clusters (Puchwein et al. 2008; Fabjan et al. 2010; McCarthy et al. 2010). While the total baryonic content of massive clusters is relatively unaffected by cooling, star formation and energy feedback, such processes can imply a quite pronounced redistribution of baryons, particularly close to the cluster centre. Duffy et al. (2010) analysed simulated haloes at $z = 0$ ranging from galaxy to cluster scales. They demonstrated that while radiative cooling increases mass concentration (see also Rudd et al. 2008), AGN feedback has the opposite effect; clusters modelled with AGN feedback have mass concentrations equal to those modelled with dark matter only. Consistent with these results, Mead et al. (2010) demonstrated that AGN feedback is able to reduce the strong lensing cross section for clusters at $z = 0.2$. Four of the five clusters they simulated had strong lensing efficiencies consistent with their dark-matter counterparts, while the fifth remained a stronger lens.

Many of the previous works investigating the role of baryons in modifying cluster cores have told similar stories: while cooling and star-formation either directly or indirectly leads to an increase of mass in the core, and therefore an increase in the strong lensing efficiency, AGN feedback negates this to some extent. Unfortunately previous studies have had limited samples of massive clusters, especially at high-redshift $z \gtrsim 0.3$, and have utilised simulations generated with values for cosmological parameters that have since been revised. The strong lensing studies of Puchwein et al. (2005), Rozo et al. (2008) and Mead et al. (2010) were undertaken in the WMAP-1 type cosmology with $\sigma_8 = 0.9$. As shown by Macciò et al. (2008), changing the cosmology from WMAP-1 to WMAP-3 best fitting models can lead to a 20% decrease in the predicted mass concentration of relaxed clusters. This is primarily due to the decrease of the power-spectrum normalisation, σ_8 , from 0.9 to 0.7, and the subsequent delay in the assembly of haloes. The current WMAP-7 best-fit values lie between these two extremes; the expected reduction in the concentration of masses considered in this work from WMAP1 to WMAP5/7 is closer to 14% (e.g. Macciò et al. 2008; Duffy et al. 2008, but see also Prada et al. 2012).

In this work we improve upon the aforementioned works by analysing the strong lensing efficiencies of a larger sample of clusters simulated within the currently favoured cosmology ($\sigma_8 = 0.8$) with only dark matter (DM), and also including the hydrodynamical treatment of gas, along with cooling, star formation and feedback from both supernova (SN) and AGN. Strong lensing properties of our fairly large sample of massive clusters are analysed at two redshifts, $z = 0.25$ and 0.5 . A description of the cosmological simulations and the cluster sample follows in Section 2. Earlier studies have characterised strong lensing by the cross section for the formation of giant arcs. A comparison with observational data requires the cross-section, as a function of source redshift, to be convolved with the source redshift distribution; uncertainties in this source redshift distribution weaken the cosmological test. We, therefore, propose that the Einstein radius is a more robust proxy for strong lensing; critical curves are determined at a single source redshift (usually $z_s = 2$), regardless of the range of source redshifts used for lens mass reconstructions. Therefore, in Section 3 and Section 4 we present the strong-lensing properties for

the relaxed sub-sample and discuss the influence of the baryonic processes; in the former section we characterise strong-lensing with the cross-section for the formation of giant-arcs, while in the latter we consider the Einstein Radii instead. At the end of this section, we describe the strong-lensing properties of unrelaxed sub-sample. These results are then interpreted in terms of variation of the density profiles induced by the presence of baryons in the simulated clusters. Finally, we summarise of our findings in Section 5.

2 SIMULATIONS

2.1 The simulated set of clusters

The set of simulated clusters analysed in this study have been previously presented by (Fabjan et al. 2010) and Bonafede et al. (2011), and a more comprehensive description will be provided in a forthcoming paper (Planelles et al. in prep), but we describe them in brief here. Cluster halos have been identified in a low-resolution simulation box having a periodic co-moving size of $1 \text{ h}^{-1} \text{ Gpc}$ for a flat ΛCDM model whose cosmological parameters were chosen as follows: present day vacuum density parameter, $\Omega_{\Lambda,0} = 0.76$; matter density parameter, $\Omega_{\text{M},0} = 0.24$; baryon density parameter, $\Omega_{\text{b},0} = 0.04$; Hubble constant $h = 0.72$; normalisation of the matter power spectrum $\sigma_8 = 0.8$; and primordial power spectrum $P(k) \propto k^n$ with $n = 0.96$. The parent simulation followed 1024^3 collision-less particles in the box. Clusters were identified at $z = 0$ using a standard *Friends-of-Friends* (FoF) algorithm, and Lagrangian regions around 24 of the clusters found to have masses $M_{\text{FOF}} > 10^{15} \text{ h}^{-1} \text{ M}_{\odot}$ were re-simulated at higher resolution employing the *Zoomed Initial Conditions* code (ZIC; Tormen et al. 1997), while resolution is progressively degraded outside these regions, so as to save computational time while still providing a correct description of the large-scale tidal field. The Lagrangian regions were large enough to ensure that only high-resolution particles are present within five virial-radii of the central cluster.

Simulations have been carried out using the TreePM-SPH GADGET-3 code, a newer version of the original GADGET-2 code by Springel (2005) that adopted a more efficient domain decomposition to improve the work-load balance. Each re-simulation has been repeated with a unique set of included baryonic processes, some of which are analysed here: one simulation-set uses collisionless dark matter particles only; one is a non-radiative run; another two implement a number of processes associated with baryons; one of these two includes AGN feedback. The basic characteristics of these re-simulation sets are described here below.

DM : simulations including only dark matter particles, that in the high-resolution region have a mass $m_{\text{DM}} = 10^9 \text{ h}^{-1} \text{ M}_{\odot}$. The Plummer-equivalent co-moving softening length for gravitational force in the high-resolution region is fixed to $\epsilon_{\text{Pl}} = 5 \text{ h}^{-1} \text{ kpc}$ physical at $z < 2$ while being fixed to $\epsilon_{\text{Pl}} = 15 \text{ h}^{-1} \text{ kpc}$ comoving at higher redshift.

NR : non-radiative hydrodynamical simulations. Initial conditions for these hydrodynamical simulations are generated starting from those of the DM-only simulations, and

splitting each particles in the high resolution region into one dark matter and one gas particle, with their masses chosen so to reproduce the assumed cosmic baryon fraction. The mass of each DM particle is then $m_{\text{DM}} = 8.47 \cdot 10^8 \text{ h}^{-1} \text{ M}_{\odot}$ and the mass of each gas particle is $m_{\text{gas}} = 1.53 \cdot 10^8 \text{ h}^{-1} \text{ M}_{\odot}$. For the computation of the hydrodynamical forces we assume the minimum value attainable by the SPH smoothing length of the B-spline interpolating kernel to be half of the corresponding value of the gravitational softening length. No radiative cooling is involved.

CSF : hydrodynamical simulations including the effect of cooling, star formation and SN feedback. Radiative cooling rates are computed by following the same procedure presented by Wiersma et al. (2009). We account for the presence of the cosmic microwave background (CMB) and for the model of UV/X-ray background radiation from quasars and galaxies, as computed by Haardt & Madau (2001). Contributions to cooling from each one of eleven elements (H, He, C, N, O, Ne, Mg, Si, S, Ca, Fe) have been pre-computed using the publicly available CLOUDY photo-ionisation code (Ferland et al. 1998) for an optically thin gas in (photo-)ionisation equilibrium. Gas particles above a given threshold density are treated as multi-phase, so as to provide a sub-resolution description of the inter-stellar medium, according to the model originally described by Springel & Hernquist (2003). Within each multi-phase gas particle, a cold and a hot-phase coexist in pressure equilibrium, with the cold phase providing the reservoir of star formation. We include a detailed description of metal production contributed by SN-II, SN-Ia and low and intermediate mass stars, as described by Tornatore et al. (2007). Stars of different mass, distributed according to a Chabrier IMF (Chabrier 2003), release metals over the time-scale determined by the corresponding mass-dependent life-times (taken from Padovani & Matteucci 1993). Kinetic feedback contributed by SN-II is implemented according to the scheme introduced by Springel & Hernquist (2003): a multi-phase star particle is assigned a probability to be uploaded in galactic outflows, which is proportional to its star formation rate. For this set of simulations we assume $v_{\text{w}} = 500 \text{ km s}^{-1}$ for the wind velocity.

AGN : the same as CSF, with a lower wind velocity of $v_{\text{w}} = 350 \text{ km s}^{-1}$, also including the effect of AGN feedback. In the model for AGN feedback, released energy results from gas accretion onto SMBHs. This model introduces some modifications with respect to that originally presented by Springel et al. (2005) (SMH hereafter), to which is largely inspired, and will be described in detail by Dolag et al. (2012, in preparation). BHs are described as sink particles, which grow their mass by gas accretion and merging with other BHs. Gas accretion proceeds at a Bondi rate, while being Eddington-limited. Once the accretion rate is computed for each BH particle, a stochastic criterion is used to decide which of the surrounding gas particles contribute to the accretion. Unlike in SMH, in which a selected gas particle contributes to accretion with all its mass, we included the possibility for a gas particle to accrete only with a slice of its mass, which corresponds to 1/4 of its original mass. In this way, each gas particle can contribute with up to four “generations” of BH accretion events, thus providing a more continuous description of the accretion process (see also Fabjan et al. 2010). BH particles are initially seeded

with a mass of $0.05 m_{\text{DM},10}$, where $m_{\text{DM},10}$ is the DM particle mass in units of $10^{10} h^{-1} M_{\odot}$. Seeding of BH particles takes place in halos when they first reach a minimum friend-of-friend (FoF) mass of $2.5 \times 10^3 m_{\text{DM},10}$ (using a linking length of 0.16 in units of the mean interparticle separation in the high-resolution region), with the further condition that such halos should contain a minimum mass fraction in stars of 0.02. The first condition on the minimum halo mass guarantees that such halos are resolved with at least $\gtrsim 200$ DM particles, while the second condition requires that substantial star formation took place in such halos. This criterion prevents seeding BHs in halos possibly located at the border of the high resolution region, which spuriously contain a low amount of cooled gas, due to the interaction with nearby low-resolution DM particles. Eddington-limited Bondi accretion produces a radiated energy which correspond to a fraction $\epsilon_r = 0.1$ of the rest-mass energy of the accreted gas, which is determined by the radiation efficiency parameter ϵ_r . The BH mass is correspondingly decreased by this amount. A fraction of this radiated energy is thermally coupled to the surrounding gas. We use $\epsilon_f = 0.05$ for this feedback efficiency, which increases to $\epsilon_f = 0.2$ whenever accretion enters in the quiescent “radio” mode and takes place at a rate smaller than one-hundredth of the Eddington limit (e.g. Sijacki et al. 2007; Fabjan et al. 2010).

2.2 The identification of clusters

The cluster haloes are identified as follows. Firstly, a standard *Friends-of-Friends* algorithm is run over the DM particles in the high-resolution regions, using a linking length of 0.16 in units of the mean-interparticle separation. Within each FoF group, we identify the position of the particle with the minimum gravitational potential, which is then taken as the centre from where clusters are then identified according to a spherical overdensity (SO) method. The virial radius is defined as the smallest radius of a sphere centred on the cluster, for which the mean density falls below the virial overdensity. The virial overdensity is measured relative to the critical density and calculated using the fitting formula of Bryan & Norman (1998), so for clusters at $z = 0.25$, $\Delta_c \approx 112$ and for clusters at $z = 0.5$, $\Delta_c \approx 129$.

Cluster haloes are chosen for our strong lensing analysis only if no low-resolution particles contaminate the region within five virial radii of the cluster centre. In Figure 1 we show the number of clusters above a given mass limit at the two redshifts considered in our analysis. Note that this is not equivalent to a halo mass function since the re-simulated regions do not cover the entire box. The sample has 42 clusters with $M_{\text{vir}} > 3 \times 10^{14} h^{-1} M_{\odot}$ at a redshift of $z = 0.25$. Moving to higher redshifts, we find 34 clusters with $M_{\text{vir}} > 3 \times 10^{14} h^{-1} M_{\odot}$ at a redshift of $z = 0.5$.

2.3 Relaxed clusters

If mergers between clusters take place along the line of sight the strong lensing efficiency can be enhanced. If the merger occurs across the sky, we will see multiple critical curves, which positively biases the cross section for giant arcs. In the case that critical curves are merging, both the Einstein radii and the cross section for giant arcs would be biased

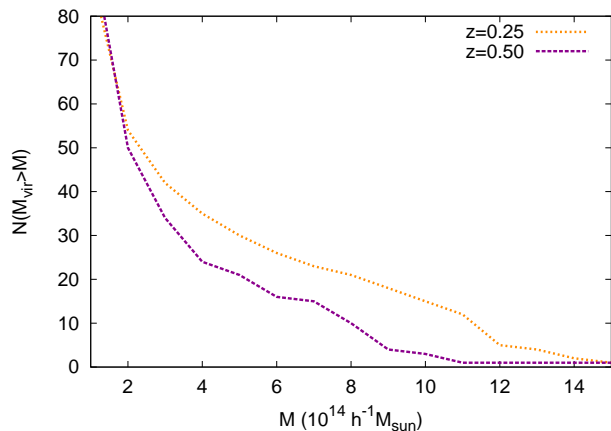


Figure 1. The cumulative virial-mass distribution of clusters in the sample at redshifts $z = 0.25$ (orange dotted curve) and $z = 0.5$ (purple dashed curve).

large. This could confuse our interpretation of the effects of baryon physics.

In order to characterise the degree of relaxation of each cluster, we compute the quantity $s_{\text{max}} = \{ \max(s_{\zeta}) : 0.05 < \zeta < 2 \}$, where

$$s_{\zeta} = \frac{|\mathbf{r}_{\text{COM}}(< \zeta R_{\text{vir}}) - \mathbf{r}_{\text{MinPot}}|}{\zeta R_{\text{vir}}}. \quad (1)$$

In the above equation, $\mathbf{r}_{\text{MinPot}}$ is the position of the particle with the minimum gravitational potential and \mathbf{r}_{COM} is the centre of mass of all the matter within ζR_{vir} . In this way, s_{ζ} represents the offset between these two measures of “centre” for any aperture radii, ζR_{vir} , so that s_{max} is the maximum offset over a range of aperture radii, which are found by allowing ζ to vary from 0.05 to 2 in 30 logarithmic steps. We define a relaxed cluster as that for which the counterpart in the DM simulation has a maximum offset parameter of $s < 0.1$.

As a visual aid, the offset parameter for each cluster at $z = 0.5$ is shown in Figure 2 plotted against the aperture radius; each curve corresponds to an individual cluster. Any cluster for which the curve exceeds the dotted line ($s_{\zeta} = 0.1$) for any radius in the given range is considered to be unrelaxed. Our adopted criterion to classify relaxed and unrelaxed clusters corresponds to similar definitions in the literature when we choose only one aperture radius, the virial radius i.e. when we set $\zeta = 1$ (e.g. Crone et al. 1996; Thomas et al. 1998; Neto et al. 2007; D’Onghia & Navarro 2007; Power et al. 2011). However, we note that adopting this common choice we would be less sensitive to complex mass distributions near the core of a cluster, which is more important in the context of strong lensing. Our definition, in a sense, weights the disturbance caused by substructure by the inverse of radial position of the substructure. In order to verify whether there is any correlation within our sample between degree of relaxation and cluster mass, we plot in Figure 3 the positions of our clusters in the $s_{\text{max}}-M_{\text{vir}}$ plane. There is negligible correlation between the cluster’s mass and the offset parameter that describes the degree of relaxation. The choice of threshold for s_{max} above which a

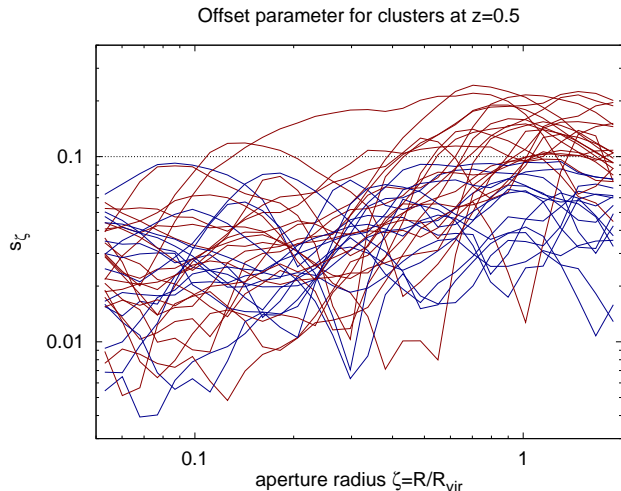


Figure 2. The offset parameter, s_ζ , as a function of aperture radius within which centre-of-mass is calculated, for all clusters at $z = 0.5$. The dotted horizontal line shows the value of the maximum offset parameter, $s_{\max} = 0.1$, allowed for a cluster to be classified as relaxed. Red and blue curves correspond to clusters which are then classified as unrelaxed and relaxed, respectively.

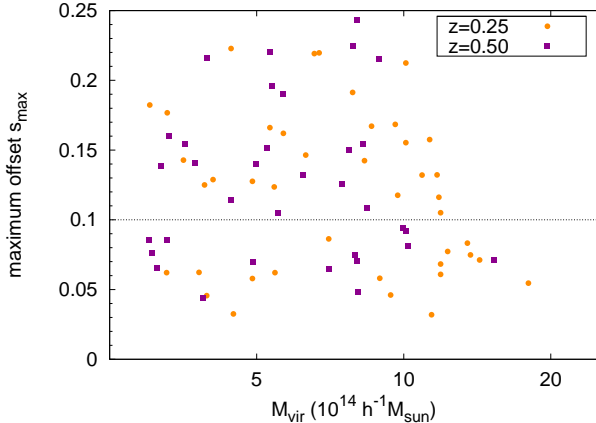


Figure 3. The relation between the maximum centre shift, s_{\max} , and the virial mass, M_{vir} , for all clusters. The orange circles represent clusters at $z = 0.25$ while the purple squares represent the clusters at $z = 0.5$.

cluster is considered unrelaxed does not appear to bias the sample in terms of mass. The total sample of 42 clusters at $z = 0.25$ includes 17 relaxed clusters, and of the 34 clusters in total at $z = 0.5$, 14 are classified as relaxed. In Section 3 and at the beginning of Section 4 we present the statistical results only for the relaxed sub-sample. In Section 4.3 we compare these results to those for unrelaxed clusters. For comparison, we note that if we had defined the relaxed sub-sample as those for which the offset at the virial radius is $s_1 < 0.07$, as is common in the literature, we would have 23 relaxed clusters at $z = 0.25$ and 12 relaxed clusters at $z = 0.5$.

3 CROSS SECTION FOR GIANT ARCS

The cross section for giant arcs is defined as the area in the source plane in which if a distant galaxy (at that redshift) was located, it would appear as a highly elongated giant arc due to the effects of strong gravitational lensing. Every line of sight through each simulated cluster will, in general, provide a unique cross section. We now describe the procedure used to calculate the giant arc cross section for each line of sight analysed for each cluster in our simulated sample. Throughout the present work, we refer to gravitational lensing quantities following the notation of Schneider et al. (1992). The lensing mass is chosen to be contributed by all particles within two virial radii of the cluster centre. We apply the thin lens approximation: the assumption that the lensing mass is constrained to a single plane. This treatment is valid for the present study, since the sizes of the cluster lenses are much smaller than D_s , D_d and D_{ds} : the angular diameter distances from the observer to the source, from the observer to the lens, and from the lens to the source, respectively. The convergence, κ , can be defined by:

$$\kappa = \frac{\Sigma}{\Sigma_{\text{crit}}}, \quad (2)$$

where Σ is the surface density and the critical surface density for gravitational lensing is given by

$$\Sigma_{\text{crit}} = \frac{c^2}{4\pi G} \frac{D_s}{D_d D_{ds}}. \quad (3)$$

Note that from here onwards, the redshift of the cluster lenses is denoted z_L , while the redshift of the background source galaxies is denoted z_s .

3.1 Calculating the lensing cross section

In order to calculate the lensing cross-section, we first measure the deflection of light-rays from background source galaxies across a field of view in which we expect to search for giant arcs. Each ray of light is deflected at the lens plane; the deflection angle is related to the convergence by:

$$\alpha(\mathbf{x}) = \frac{1}{\pi} \int_{\mathbb{R}^2} d^2 x' \kappa(\mathbf{x}') \frac{\mathbf{x} - \mathbf{x}'}{|\mathbf{x} - \mathbf{x}'|^2}, \quad (4)$$

where \mathbf{x} is a dimensionless position in the lens plane. It is possible to choose the scaling such that the gravitational lens equation is given by:

$$\boldsymbol{\beta} = \boldsymbol{\theta} - \boldsymbol{\alpha}(\boldsymbol{\theta}), \quad (5)$$

where $\boldsymbol{\beta}$ is the angular source position and $\boldsymbol{\theta}$ is the angular position of the image on the sky. Producing maps of the deflection angle at each grid point requires a few steps, as shown in the cartoon diagram in Figure 4. We describe the procedure below. The angular and spatial resolutions are quoted for sources at $z_s = 2$ and clusters at $z_L = 0.25$, but quantities for clusters at $z_L = 0.5$ are given in square brackets. The lensing mass is projected onto one of two possible lens planes, depending on the position of the particles. Those that lie at a projected co-moving distance of more than $0.9 \text{ h}^{-1} \text{ Mpc}$ [$1.35 \text{ h}^{-1} \text{ Mpc}$] from the cluster centre are placed on a low-resolution 2048×2048 grid. The angular resolution of this grid is 1.7 arcsec [0.9 arcsec]. Particles that are projected closer to the cluster core, and are therefore responsible for the bulk of the strong lensing, are placed on

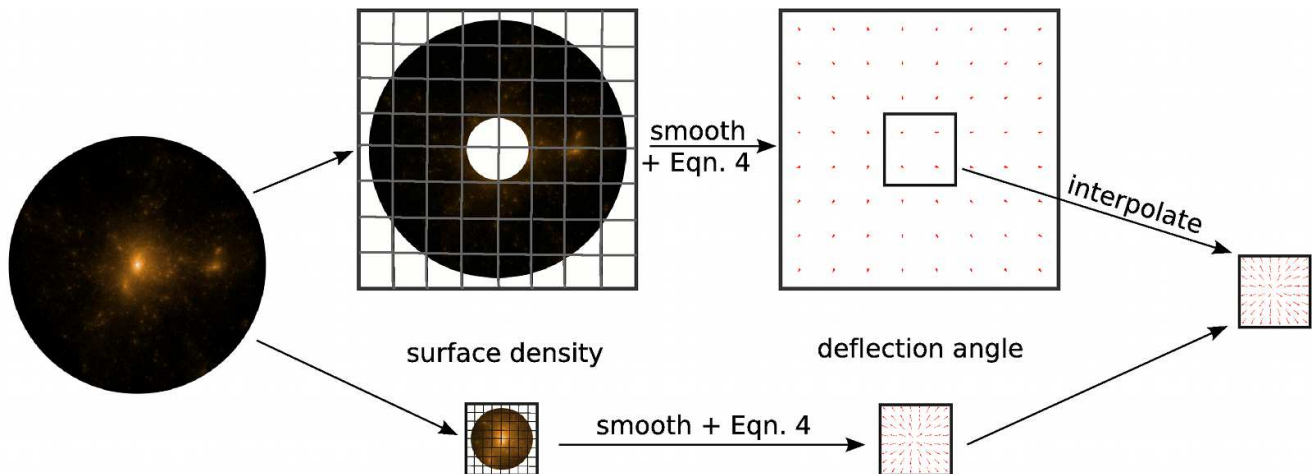


Figure 4. A cartoon diagram describing the calculation of deflection angle, α , across a high resolution grid. The lensing mass is divided into two parts: an inner and an outer region (shown in the bottom and top rows, respectively), each of which are projected onto a small high-resolution and large low-resolution grid, respectively. The surface density distribution on each grid, κ , is smoothed, then the deflection angle is calculated using equation 4. The total deflection angle is the sum of these two. However the deflection angle calculated in the inner region of the large grid must first be interpolated onto the small high-resolution grid. See text for further details

a high-resolution 2048×2048 grid. The angular resolution of this grid is 0.3 arcsec [0.2 arcsec]. The mass on each grid is smoothed with a truncated Gaussian filter of size $\sigma = 5 h^{-1} \text{kpc}$, to match the force-softening length of the simulation. The size of each grid is sufficiently larger than the projected extent of the mass on that grid, so that smoothing does not result in any loss of mass.

We convolve each of the two convergence maps with the appropriate kernel from equation 4. This leaves us with two maps of the deflection angle: one at high-resolution where the deflection is solely due to the mass in the projected cluster core; the other at low-resolution from the rest of the lensing mass. For the subsequent ray-shooting procedure, we use a single map of deflection angle for each cluster projection; the final map has the same size and resolution as the high-resolution grid described above. The deflection angle at each grid point is determined with bilinear interpolation from the closest grid-points of the low-resolution map, and adding the corresponding grid-point from the high-resolution map. The resulting deflection angle map has an angular resolution of 0.3 for clusters at $z_L = 0.25$ and 0.2 for clusters at $z_L = 0.5$.

Calculating the cross-section for giant arc formation requires a ray-shooting and arc-identifying procedure, which has been previously presented in Meneghetti et al. (2000) and Meneghetti et al. (2005). Elliptical sources with an equivalent radius of size 0.5 are placed throughout the source plane; more sources are placed in regions identified as caustics. The deflection angle maps allow mock images to be generated from the sources. The images are fitted to ellipses and the length-to-width ratio, L/W , is determined. If L/W surpasses some threshold elongation, η , the image is identified as a ‘giant arc’. The cross-section for giant arc formation, σ_η , is the area in the source plane covered by sources that are mapped onto giant arcs. For the present study, the length-to-width threshold is chosen to be $\eta = 7.5$ — following Puchwein et al. (2005), Mead et al. (2010) and Meneghetti et al. (2011) — because much larger cross-sections are subject to small number statistics, and

much smaller cross-sections are too sensitive to the intrinsic ellipticities of the source galaxy. We discuss other choices of threshold of Section 3.2.

We present results in this section and Section 4 for sources at redshift $z_s = 2$, but include the statistical results for a source redshift of $z_s = 1$ in Table 1. For these lower source redshifts, we would expect smaller Einstein radii, so the deflection angle maps have a higher angular resolution: 0.2 for clusters at $z_L = 0.25$ and 0.1 for clusters at $z_L = 0.5$.

3.2 The impact of baryons on the cross section for giant arcs

The baryonic processes as implemented in the hydrodynamical simulations affect the details of the structure of each cluster halo. Figure 5 shows a single cluster of mass $M_{\text{vir}} = 8 \times 10^{14} h^{-1} M_\odot$ in our $z_L = 0.5$ sample as found in each of the four re-simulations. The basic structure is recognisable in each simulation and the subhaloes appear in much the same positions, as seen in the convergence maps along the top row. However, the distribution of matter near the clusters centre is sufficiently altered by baryonic physics so that the caustics, as shown in the bottom row of the same figure, are distinct. In particular, note that the CSF simulation produces larger source caustics, shown in blue, and larger tangential image caustics — or critical curves — shown in red. The tangential part of the image caustic extends around a substructure that was sub-critical in the other simulations. For this particular cluster, as seen from one line of sight, the strong lensing efficiency is highest when the cluster is generated within the CSF simulation.

It is our aim to determine whether this is generally true for simulated galaxy clusters, and in particular, how the strong lensing properties predicted by the AGN simulations compare with the other simulations. We have a large sample of galaxy cluster, but we should not consider only one line of sight through each cluster. Due to the aspherical nature of clusters, as well as the presence of substructure, each line of

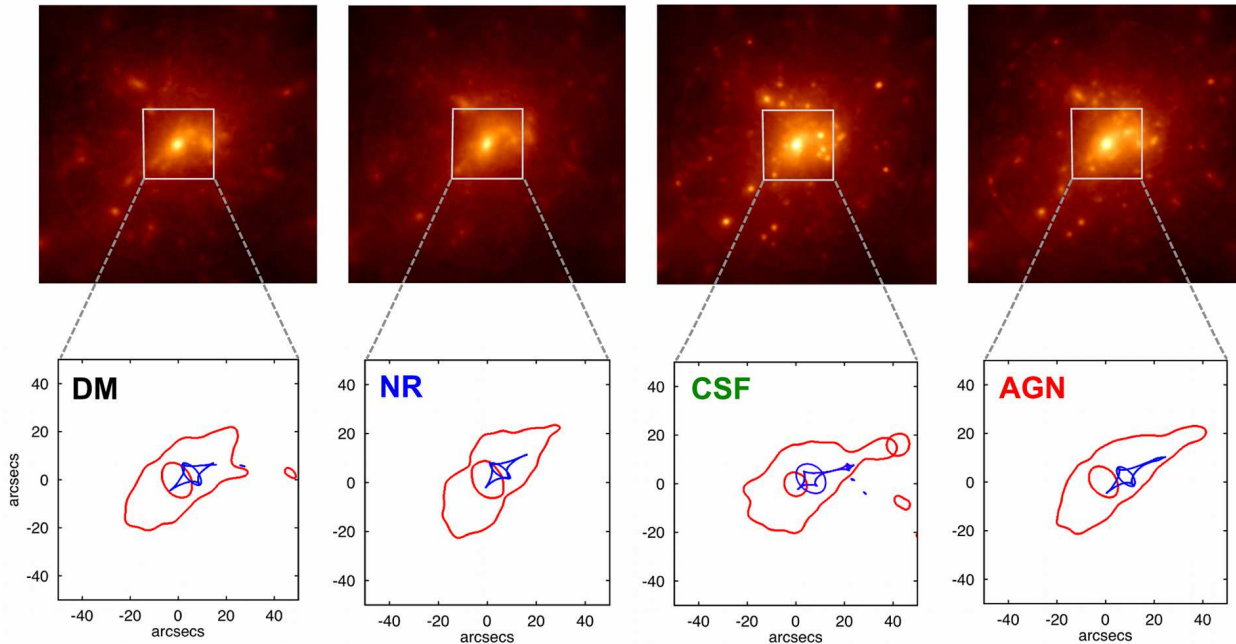


Figure 5. One cluster at $z_L = 0.5$ seen from the same viewpoint within different simulations: DM (left panel), NR (second panel), CSF (third panel), and AGN (right panel). Along the top row, we show the convergence map of the cluster, ~ 410 arcsecs across, in which brighter region represent higher surface densities; along the bottom row is the corresponding source caustic in blue and image caustic, a.k.a the critical curve, in red, both determined for a source at redshift $z_s = 2$

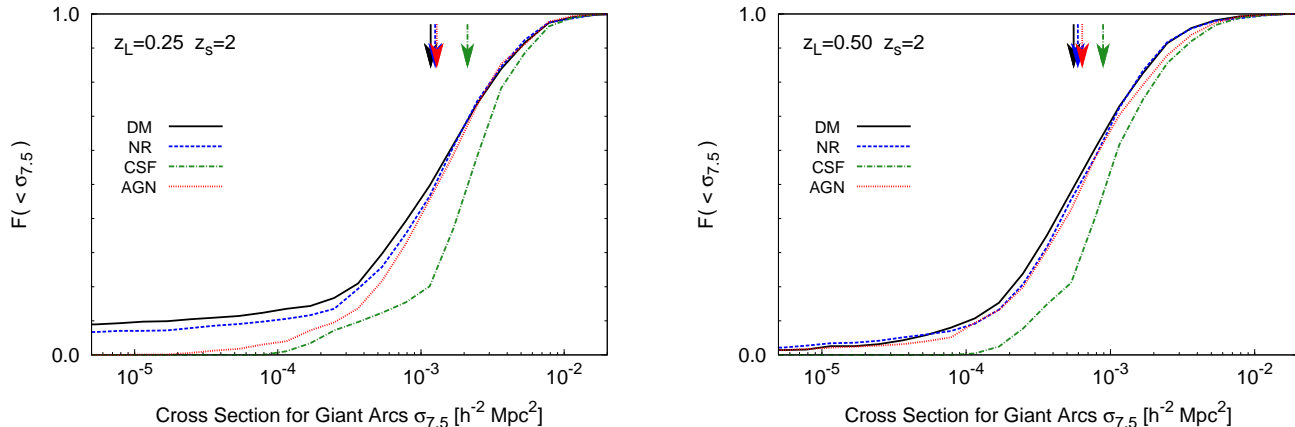


Figure 7. The cumulative probability distribution for the source-plane cross-section for the formation of giant arcs combining 50 lines of sight through the relaxed clusters at $z_L = 0.25$ (left panel) and $z_L = 0.5$ (right panel). Different lines and colours have the same meaning as in Figure 6. The arrows mark the median values of the $\sigma_{7.5}$ cross section for the models.

sight produces a unique cross section. Therefore, each cluster is associated with a distribution of possible cross sections (see, for example, figure 3 of Dalal et al. 2004). In Figure 6, we show such a distribution by measuring the cross section, $\sigma_{7.5}$, for 50 lines of sight through one cluster in our sample, also seen in Figure 5. In the present study, we analyse projections of each cluster along 50 randomly chosen lines of sight. The results for all our sets of simulated clusters are combined in the left-hand panel of Figure 7.

We conduct a two-sample Kolmogorov-Smirnov test to compare the probability distribution of $\sigma_{7.5}$ values for each simulation against the same distribution for the DM simula-

tions. The D-statistic is the maximum difference between the two cumulative probability distributions. Ideally we would like to determine the probability, p_σ , that the D-statistic would be at least as large as that measured assuming the samples are drawn from the same underlying distribution. We recognise that while the clusters are independent, the many lines of sight analysed for each cluster are not independent from each other. In an actual observational sample, one would measure a single strong-lensing efficiency for each cluster; however using a simulated sample, scatter due to orientation has to be taken into account. Therefore, stacking the results for all lines of sight analysed, we calculate

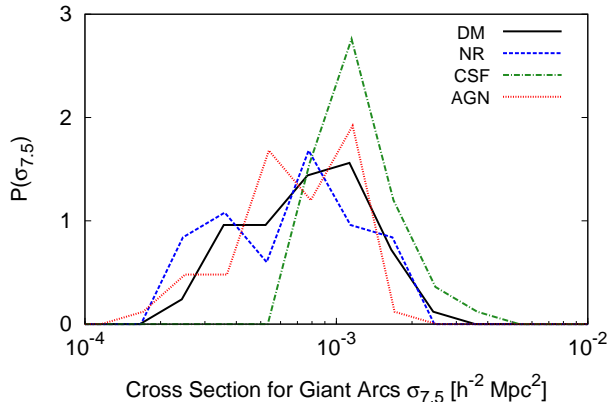


Figure 6. The probability distributions for the cross section that would be measured for a single simulated cluster at $z_L = 0.5$ for a source redshift of $z_s = 2$; the cluster is the same as that shown in Figure 5. Different curves refer to the distributions produced by the four different simulations: DM (black solid line), NR (blue dashed line), CSF (green dash-dotted line), AGN (red dotted line)

the D-statistic. Using the total number of lines of sight (50 times the number of clusters) as the ‘sample size’ provides a lower limit for the p-value, p_σ^{min} . Alternatively, by letting the number of clusters be the ‘sample size’, we can obtain an upper limit on the p-value, p_σ^{max} . Both are listed in Table 1. If the clusters were all perfectly spherically symmetrical, so that all lines of sight resulted in the same value of $\sigma_{7.5}$, then p_σ^{max} would be equivalent to the required p_σ .

Table 1 also include the typical cross-sections for clusters in each simulation, for low and high source redshifts: $z_s = 1$ and $z_s = 2$. These are calculated by taking the median value of the cross-section over the 50 lines of sight analysed for each clusters, then averaging over all clusters. Comparing the results for DM and NR simulations, we find that the ability to lens background galaxies into giant arcs is similar, independently of whether the cluster lens is simulated with collision-less particles only, or with additional non-radiative gas. As seen for the CSF simulation, when cooling and star-formation are implemented, the cross-section for the formation of giant arcs is boosted by a factor of ~ 1.5 for high source redshifts ($z_s = 2$) and ~ 2 for lower source redshifts ($z_s = 1$). This is a slightly smaller ‘boost’ relative to the findings of Puchwein et al. (2005), Rozo et al. (2008) and Mead et al. (2010). This difference with respect to previous simulation models can be understood in terms of the more efficient SN feedback implemented in our CSF simulation set, which more efficiently counteracts the effect of halo contraction induced by cooling. In fact, Puchwein et al. (2005) use the same model for galactic ejecta, but with a smaller velocity of galactic winds, with $v_w = 350 \text{ km s}^{-1}$. Furthermore, Rozo et al. (2008) and Mead et al. (2010) only include thermal schemes for SN feedback, which are rather inefficient in regulating cooling at the centre of cluster-sized halos.

AGN feedback reduces the giant-arc cross-section and makes it comparable to the predicted cross-section from collision-less simulations. When we compare clusters modelled with dark matter only (DM results shown in black) and their counterparts modelled with the complete set of bary-

onic processes, including AGN feedback (AGN shown in red), we find surprisingly little difference in the typical cross-sections for clusters at $z_L = 0.25$ - now a boost of only ~ 10 per cent. However, at $z_L = 0.5$ clusters modelled with AGN feedback are ~ 30 per cent more efficient at lensing background galaxies into giant arcs. Given the results for Einstein radii (see Section 4.2 below), this is likely due to the presence of substructures that produce additional arcs rather than the re-distribution of mass near the cluster centre. The difference in the results between CSF and the AGN simulations arise from a combination of the reduced SN wind-speed and the introduction of thermal AGN feedback. However, if the CSF simulations had a similarly reduced wind-speed, the reduced feedback efficiency would lead to increased cooling and a higher lensing cross-section, therefore it is the AGN feedback that is responsible for reducing the lensing efficiency. Mead et al. (2010) analysed three projections for each of five clusters at $z_L = 0.2$ with similar simulation sets. For four of these five clusters the strong lensing cross-sections for the dark matter simulation and their AGN simulation were very similar. At this redshift, given the small sample and number of projections, this is consistent with our findings.

As described earlier, images are identified as arcs if their length-to-width ratio surpasses the threshold elongation, η . Although extreme values for this threshold are not useful, the exact value is somewhat arbitrarily chosen; to be sure that the results are not qualitatively affected by this choice, we plot the cross section as a function of η in Figure 8. The lines represent the median cross section over the 50 lines of sight for each individual cluster, then averaged over all the clusters in the (relaxed) sample. The error bars represent the 16th and 84th percentile for individual clusters, then averaged over all the clusters. These error-bars, therefore, reflect the triaxiality of the clusters. Unsurprisingly, a larger and more extreme choice of threshold allows a smaller cross section, since less sources would be able to produce such long and thin arcs, but the qualitative differences between the different simulation sets are the same.

By comparing the error-bars in Figure 8 for all re-simulations, we find that as in Rozo et al. (2008), the spread in the distribution of possible cross-sections is also reduced significantly in the CSF simulations. These clusters are less susceptible to light-of-sight effects than those modelled with dark matter only or non-radiative gas, predominantly due to the more spherical shape of the clusters resulting from the condensing of baryons and the subsequent response from the dark matter component (Blumenthal et al. 1986; Gnedin et al. 2004; Kazantzidis et al. 2004; Bryan et al. 2012). The steeper inner profile (see Section 4.4) makes the clusters less susceptible to coincidental mass along the line of sight. Although AGN feedback regulates the isotropic condensation of baryons, the reduced spread in cross-sections is also found for the AGN clusters, particularly at $z_L = 0.5$.

Figure 9 shows the giant arc cross-section, $\sigma_{7.5}$, plotted against the mass of each clusters. Each cluster is represented as a single point in the graph, with different colours representing the counterparts in the four re-simulations. The error-bars mark the 16th and 84th percentiles of $\sigma_{7.5}$ found over the 50 lines of sight analysed. The figure suggests that there exists a scaling relation between lensing efficiency and mass, but that the correlation is tighter at

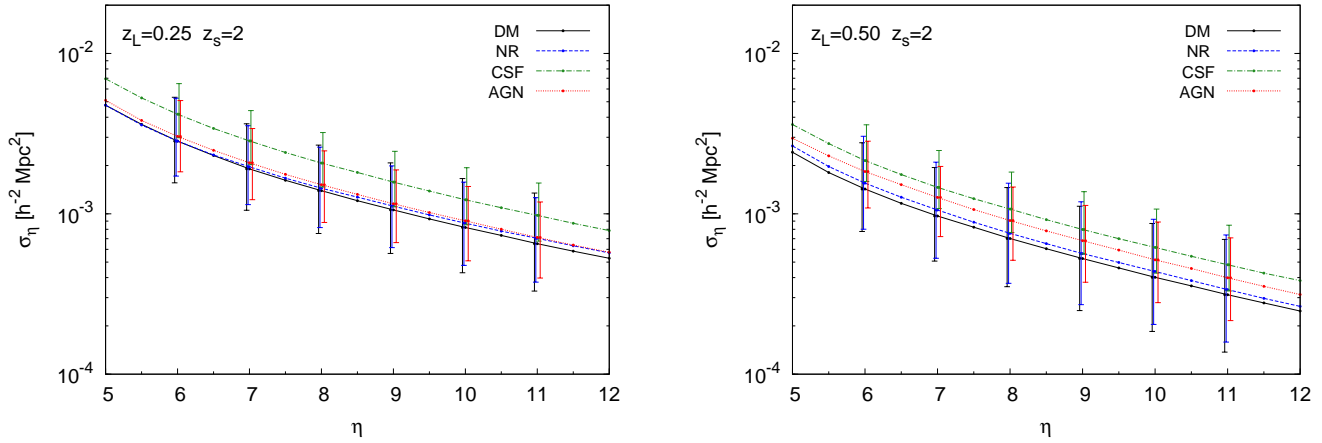


Figure 8. The giant arc cross section plotted against chosen elongation threshold η for the relaxed cluster sub-sample at $z_L = 0.25$ (left panels) and $z_L = 0.50$ (right panels). The cross section for a given value of η is the median of 50 lines of sight through each cluster, then averaged over all clusters. The errorbars mark the 16th and 84th percentile for each cluster, then averaged over all clusters. The source redshift is $z_s = 2$

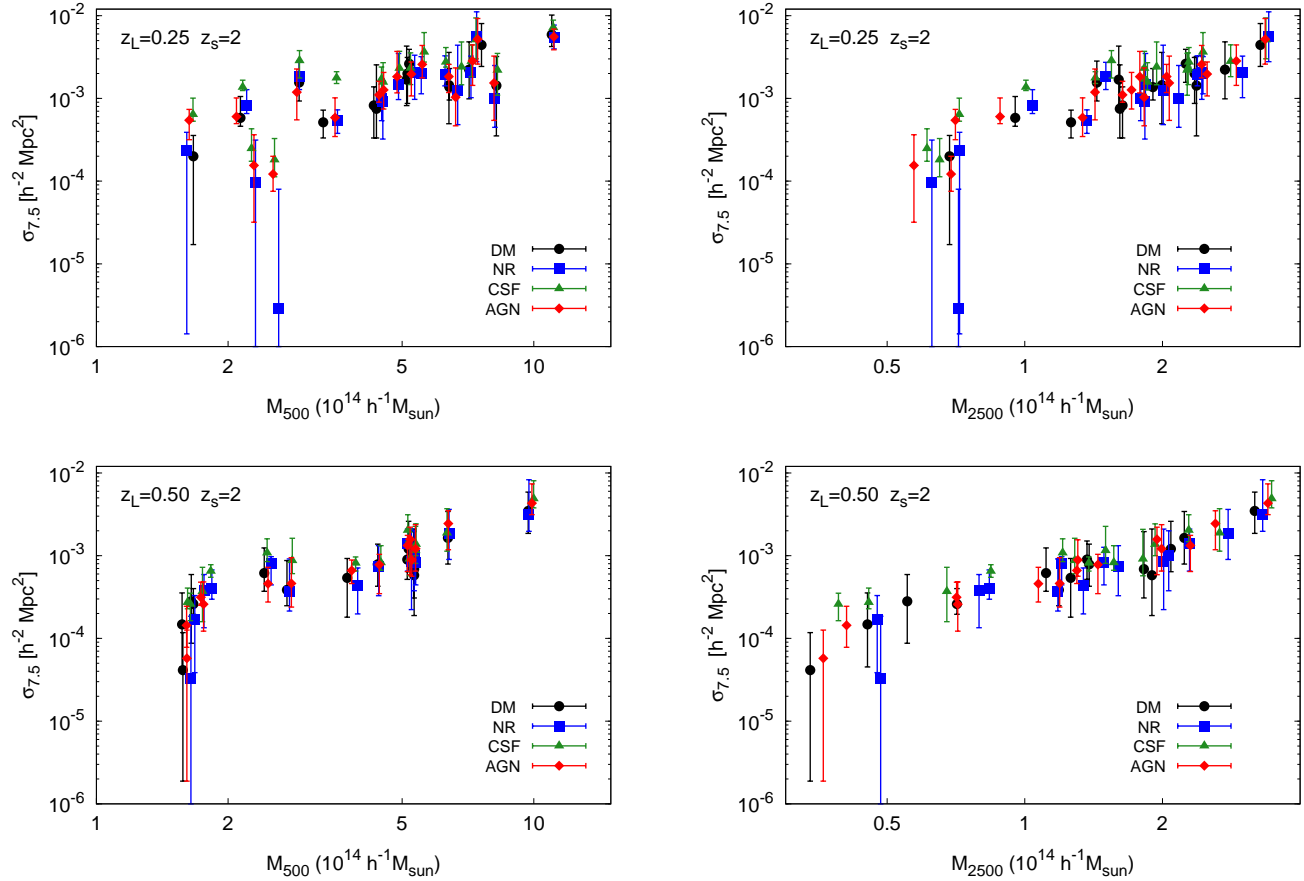


Figure 9. The cross-section for the formation of giant arcs at source redshift of $z_s = 2$ as a function of cluster mass, for our relaxed cluster sub-sample. Each dot represents the median cross-section from the 50 lines of sight analysed for a single cluster, while the error bars mark the 16th and 84th percentiles. In the left-hand panels, the characteristic mass is M_{500} while for the right-hand panels, the characteristic mass is M_{2500} . The clusters at $z_L = 0.25$ are shown on the top row while the clusters at $z_L = 0.50$ are shown on the bottom row.

Table 1. Statistical Analysis of Strong Lensing Properties of Relaxed Clusters. Column 1: simulation set. Columns 2 and 3: redshifts of the lens, z_L , and of the source, z_s . Column 4: Pearson correlation coefficient r for the $\log(\sigma_{7.5})$ – $\log(\theta_E)$ relation. Column 5 and 6: least-squares fit to the $\log(\sigma_{7.5})$ – $\log(\theta_E)$ relation (see Eqn. 6). Column 7: typical value of the Einstein radius, θ_E , computed as the median value over 50 lines of sight through each cluster, then averaged over all clusters (units of arcseconds). Columns 8 and 9: values of p_θ^{min} and p_θ^{max} , defined as the lower and upper limits, respectively, of a true p -value from a KS-test performed to compare the θ_E probability distribution of each simulation set against the corresponding result for the DM simulation. Column 10: the typical cross section for the lensing of galaxies at z_s into giant arcs with elongation $\eta = 7.5$, $\sigma_{7.5}$, defined as the median value over 50 lines of sight through each cluster, then averaged over all clusters (units of $10^{-4}h^{-2}\text{Mpc}^2$). Columns 11 and 12: the same as in columns 8 and 9, respectively, but to compare the $\sigma_{7.5}$ probability distribution.

Simulation	z_L	z_s	r	a	b	θ_E	p_θ^{min}	p_θ^{max}	$\sigma_{7.5}$	p_σ^{min}	p_σ^{max}
DM	0.25	2	0.94	2.15 ± 0.02	-6.04 ± 0.03	29	–	–	16	–	–
NR	0.25	2	0.92	1.93 ± 0.03	-5.70 ± 0.04	30	0.02	1.00	17	0.11	1.00
CSF	0.25	2	0.97	2.02 ± 0.02	-5.72 ± 0.03	33	$< 10^{-5}$	0.87	24	$< 10^{-5}$	0.35
AGN	0.25	2	0.97	2.11 ± 0.02	-5.96 ± 0.03	30	1×10^{-4}	1.00	18	3×10^{-4}	1.00
DM	0.5	2	0.96	2.10 ± 0.02	-5.90 ± 0.03	20	–	–	8.2	–	–
NR	0.5	2	0.95	2.08 ± 0.02	-5.89 ± 0.03	21	0.11	1.00	8.9	0.14	1.00
CSF	0.5	2	0.96	1.87 ± 0.02	-5.45 ± 0.03	21	7×10^{-5}	1.00	12.4	$< 10^{-5}$	0.59
AGN	0.5	2	0.96	2.09 ± 0.02	-5.84 ± 0.03	21	0.93	1.00	10.6	0.07	1.00
DM	0.25	1	0.94	2.02 ± 0.02	-5.92 ± 0.03	21	–	–	5.0	–	–
NR	0.25	1	0.91	1.81 ± 0.03	-5.65 ± 0.04	22	0.008	1.00	5.6	0.16	1.00
CSF	0.25	1	0.96	2.10 ± 0.02	-5.92 ± 0.03	25	$< 10^{-5}$	0.80	10.5	$< 10^{-5}$	0.11
AGN	0.25	1	0.95	2.18 ± 0.02	-6.14 ± 0.03	22	$< 10^{-5}$	0.99	6.1	$< 10^{-5}$	1.00
DM	0.5	1	0.89	2.21 ± 0.04	-6.13 ± 0.04	9	–	–	1.6	–	–
NR	0.5	1	0.88	2.29 ± 0.04	-6.29 ± 0.05	10	4×10^{-4}	1.00	1.5	0.20	1.00
CSF	0.5	1	0.93	2.02 ± 0.03	-5.78 ± 0.03	12	$< 10^{-5}$	0.46	2.9	$< 10^{-5}$	0.25
AGN	0.5	1	0.92	2.32 ± 0.03	-6.22 ± 0.04	10	$< 10^{-5}$	0.95	2.2	$< 10^{-5}$	0.99

higher-overdensities; this reflects the region most responsible for strong lensing. The higher scatter when $\sigma_{7.5}$ is plotted as a function of M_{500} reflects the fact that different re-simulations create differing distributions of baryons in the cluster core, when comparing clusters at a fixed mass at lower overdensities.

4 EINSTEIN RADII

The cosmological test based on arc statistics is subject to uncertainty in the characteristics of the source population. Performing a comparison with observed arc statistics requires one to convolve the predicted giant arc cross-section with an assumed redshift distribution for the background galaxies. The uncertainties in this redshift distribution creates an additional uncertainty in the cosmological test. This additional uncertainty is unnecessary since one might instead characterise strong lensing efficiency by the angular scale which separates highly magnified images; this is known as the Einstein radius. Measuring the Einstein radii requires the observer to: measure the shape and redshift of a reasonable number of highly magnified high redshift sources, reconstruct the lens mass distribution, and infer the critical curves at a single redshift. This is achievable even if the various sources are at different redshifts, and bypasses the need to independently measure the expected number density and redshift evolution of the sources. We therefore measure the Einstein radii for our cluster sample and compare the results between the different re-simulations.

4.1 Measuring the Einstein Radius

The angular separation of highly magnified background galaxies has a formal definition, which is strictly applicable only in the case of axially symmetric lenses. However, galaxy clusters are not axially symmetric in general; there exist a number of different definitions in the literature for how one might calculate the Einstein radius for more realistic lenses. For example, one might divide the area enclosed within the tangential critical curve by π , as per the so-called ‘equivalent Einstein radius’ definition used, e.g., by Puchwein & Hilbert (2009), Zitrin et al. (2011) and Redlich et al. (2012). On the other hand, Broadhurst & Barkana (2008) define the ‘effective Einstein radius’ as the radius that encloses a mean surface density equal to the critical surface density $\kappa = 1$ (see Puchwein & Hilbert 2009 for further discussion on how these two definitions compare). We, instead, follow the definition of Meneghetti et al. (2011) and characterise our statistics by a ‘median Einstein radius’: the median distance of the tangential critical points from the clusters centre. Meneghetti et al. (2011) has demonstrated that the median Einstein radius has a tighter correlation with strong lensing cross section than the ‘equivalent Einstein radius’. When measuring the Einstein radius, Meneghetti et al. (2011) define the cluster centre to be the location of the maximum of the projected mass distribution. In the present work, we define the centre to be the projected position of the particle in the simulated cluster with the lowest potential. This is done in order to avoid attributing the position of the centre to a subhalo in cases in which such a subhalo is fortuitously

projected so it has a higher projected mass density than the centre of the main halo.

We use the high resolution deflection-angle map (as described in Section 3.1) to identify tangential critical points within the same field of view at the same angular resolution. There can be complications in the presence of substructure, which require one to discard some of the critical points before measuring the Einstein radius. We show an unrelaxed cluster in Figure 10 as an example. There is a large substructure present and, from some lines of sight, visible within the field of view. For each line of sight analyzed, critical points are mapped out across the lens plane forming a ‘critical curve’ also known as an image caustic; these correspond to the caustics in red. Then, critical points associated with the tangentially sheared images (as opposed to radially sheared) at the ‘primary’ critical curve around the centre of the cluster are identified, so that ‘secondary’ critical curves associated with substructure do not bias the measurement. These are the ‘cleaned’ curves shown in black. The projected distance of each ‘clean’ point from the cluster centre is measured; the Einstein radius, θ_E , is the median value over all these points.

If the secondary critical curve merges with the primary, as shown in the bottom row of Figure 10, they cannot be distinguished, and θ_E is artificially increased. The cross-section $\sigma_{7.5}$ gives, to a first approximation, the region enclosed by the source caustics (shown in blue). The measurement of $\sigma_{7.5}$ can be artificially enhanced by the presence of substructure. We discuss this further in Section 4.3. For a relaxed cluster, there would be fewer lines of sight in which the secondary and primary critical curves merge, and the cluster will have smaller secondary critical curves which have a less significant impact on the measurement of $\sigma_{7.5}$ and θ_E .

Figure 11 shows the giant-arc cross section and the Einstein radii for corresponding lines of sight through each cluster. As in Meneghetti et al. (2011), it is clear that the correlation is very strong for our relaxed cluster subsample. We perform a least-squares fitting to a function of the form:

$$\log(\sigma_{7.5}) = a \log(\theta_E) + b, \quad (6)$$

and measure the Pearson correlation coefficient for each simulation separately, including only lines of sight with non-zero values for both the cross section and Einstein radii. The results for a , b and r are summarised in Table 1. The correlation coefficient, r , ranges from 0.92 to 0.97 for the relaxed clusters at $z_L = 0.25$, and from 0.95 to 0.96 for the relaxed clusters at $z_L = 0.5$. Two of the clusters in the NR simulation are responsible for highly elliptical critical curves and elongated source caustics, which results in the scatter above the line of best-fit in the left panel of Figure 11, and makes the line of best-fit shallower; this is indicative of the sensitivity of the fit to substructure. Similarly, a recent study by Redlich et al. (2012) has concluded that the presence of substructure and cluster mergers in the Meneghetti et al. (2011) simulated clusters sample — as opposed to semi-analytic smooth triaxial cluster-halo models — results in shallower slope and higher normalisation. The line of best-fit to Eqn. 6 for the NR simulation at $z_L = 0.5$ and $z_s = 2$ is the most appropriate for comparison to the results of Meneghetti et al. (2011), which are obtained using the $z > 0.5$ clusters found in the non-radiative *MareNostrum* simulation. Compared to Meneghetti et al. (2011) we find a lower normalisation, a ,

and a steeper slope, b , of the $\log(\sigma_{7.5})$ – $\log(\theta_E)$ relation. This can be attributed to our deliberate exclusion of clusters with significant substructure and merger-activity in our relaxed subsample.

We can expect the slope of the $\log(\sigma_{7.5})$ – $\log(\theta_E)$ relation to reflect the inner mass profile of the lens (Redlich et al. 2012). Dark-matter haloes, such as those in DM simulations, follow NFW profiles (Navarro et al. 1996), with inner density profiles that fall off as $\rho(r) \propto r^{-1}$. In clusters with significant gas cooling, such as those in the CSF simulations, the density profile is close to isothermal ($\rho \propto r^{-2}$), and so, produce a large tangential magnification relative to radial magnification, and therefore a boost in $\sigma_{7.5}$ compared to the DM clusters. Since the positions of the critical points are relatively stable to the inner slope — assuming no significant redistribution of mass to larger radii — there is a greater boost in the giant arcs cross section as opposed to Einstein radius, particularly for low mass lenses (see figure 5.7 in Oguri 2004), which results in a shallower slope in the $\log(\sigma_{7.5})$ – $\log(\theta_E)$ relation, and a smaller value of a . For low source redshifts, lensing efficiencies are lower, resulting in greater scatter as the source sizes approach the resolution of the lensing maps; the line of best-fit is sensitive to this scatter and less sensitive to the inner mass profiles.

4.2 The impact of baryons on the Einstein radii

We plot the cumulative probability distribution for Einstein radii in Figure 12 combining all 50 lines of sight through each of the relaxed clusters. As in Section 3.2, we conduct a two-sample Kolmogorov-Smirnov test to compare the probability distribution for each simulation against the DM simulation. We want to determine the probability, p_θ , that the D-statistic would be at least as large as that measured assuming the samples are drawn from the same underlying distribution. As noted before, while the clusters are independent, the many lines of sight analysed for each cluster are not independent from each other. However, for the simulated sample, scatter due to orientation has to be taken into account. Stacking the results for all lines of sight analysed, we calculate the D-statistic. Defining the ‘sample size’ as the total number of lines of sight (50 times the number of clusters) provides a lower limit for the p-value, p_θ^{min} . Alternatively, by letting the number of clusters be the ‘sample size’, we can obtain an upper limit on the p-value, p_θ^{max} . Both are listed in Table 1.

Table 1 also includes the typical Einstein radii for clusters in each simulation, for low and high source redshifts: $z_s = 1$ and $z_s = 2$. These are calculated by taking the median value of the Einstein radius over the 50 lines of sight analysed for each cluster, then averaging over all clusters. The strong lensing efficiency of a cluster is sensitive to the enclosed mass within θ_E . Therefore, lens-source configurations that produce larger Einstein radii are less susceptible to the effects of baryons, since AGN lead to the re-distribution of mass within reasonable small radii; we leave a more detailed discussion to Section 4.4. Comparing the results for DM and NR simulations, we find that Einstein radii are similar whether the cluster lens is simulated with collision-less particles only, or with additional non-radiative gas. Comparing the results for DM and CSF simulation, gas cooling and star formation increase the predicted Einstein

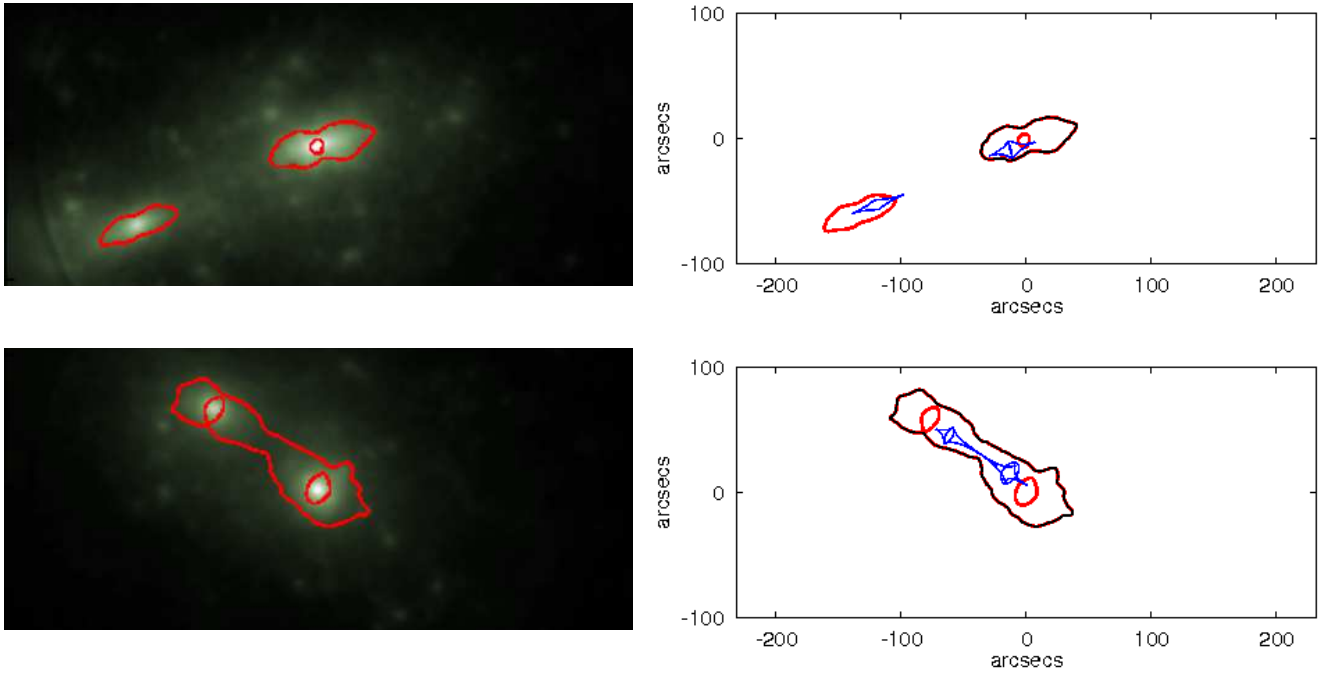


Figure 10. The surface density map (left-hand panels) and image and source caustic (right-hand panels) of an *unrelaxed* $z_L = 0.5$ cluster in our sample. In the left-hand panels, brighter regions correspond to higher surface density and the image caustic is overlaid in red. In the right-hand panels, the image caustic is shown in red, with the ‘cleaned’ caustic - used to infer the Einstein radius - drawn in black, and the source caustic at $z_s = 2$ shown in blue. The ‘primary’ image caustic is associated with the centre of the cluster, while a large substructure present within the field of view produces a ‘secondary’ image caustic. Seen from one line of sight (top row), the secondary caustic is distinct, so the cleaned caustic captures only the primary caustic, while from the other line of sight (bottom row) the primary and secondary caustics are merged, so the cleaned caustic captures both, and artificially enhances the inferred Einstein radius.

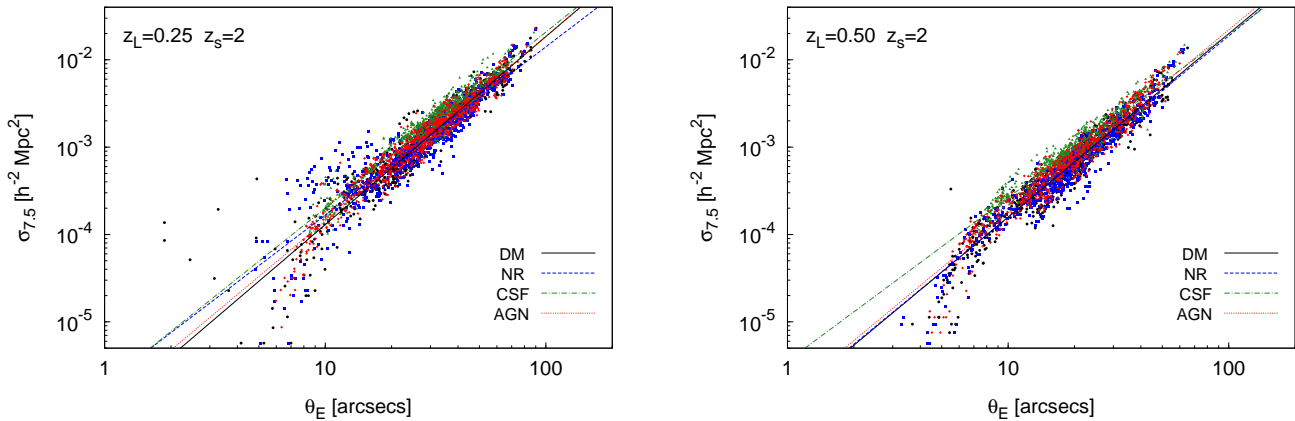


Figure 11. Relationship between the giant-arc cross section, $\sigma_{7.5}$, and the Einstein radius, θ_E , for each of the 50 orientations of each cluster. On the left panel, we show the results from the clusters at $z_L = 0.25$ and on the right panel, we show the results from the clusters at $z_L = 0.50$; both are for source redshift of $z_s = 2$. Results for the four simulations are combined: dark matter only (black); dark matter and non-radiative gas (blue); with cooling and star-formation (green); and with AGN feedback (red)

radii by ~ 10 per cent for high source redshifts ($z_s = 2$) and ~ 20 – 40 per cent for lower source redshifts ($z_s = 1$). This effect is more significant for lower source redshifts, for which the Einstein radii are typically smaller. With the inclusion of AGN feedback, the typical Einstein radii are reduced with respect to the CSF case. For Einstein radii calculated for source redshifts of $z_s = 2$, the fractional increase relative

to the clusters in the DM simulations is only ~ 5 per cent. This is the source redshift that reconstructed critical curves are commonly scaled to in observational studies. The greatest difference between predicted Einstein radii from DM and AGN simulations occurs for high- z clusters and low- z sources, which corresponds to the smaller Einstein radii ($\theta < 20''$).

Figure 13 shows the Einstein radius for each cluster as

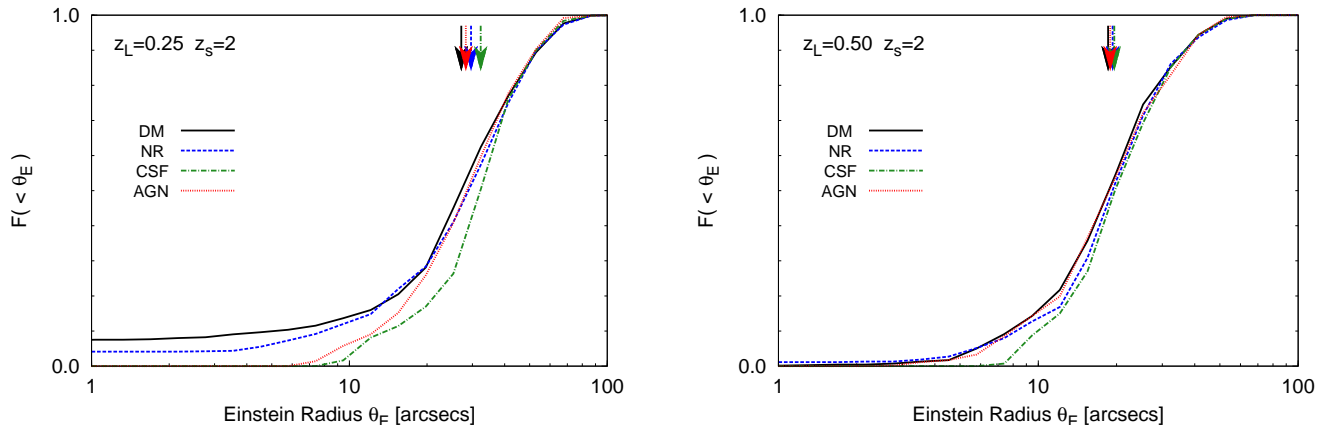


Figure 12. The cumulative distribution of Einstein radii obtained by combining 50 lines of sight through each of the relaxed clusters in the sample. The source redshift is assumed here to be $z_s = 2$. On the left panel, we show the results for the 24 relaxed clusters with $M_{\text{vir}} > 3 \times 10^{14} h^{-1} M_\odot$ at redshift $z_L = 0.25$. On the right panel, we show the results for the 18 relaxed clusters above the same mass limit at redshift $z_L = 0.5$

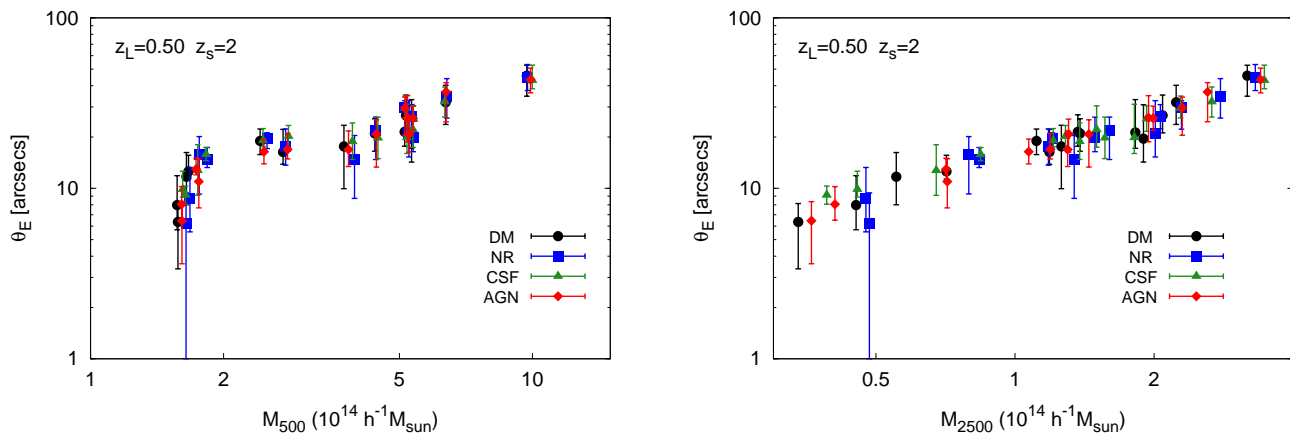


Figure 13. The Einstein radius for a source redshift of $z_s = 2$ versus cluster mass combining 50 lines of sight through the relaxed clusters at $z_L = 0.5$. For the left-hand panels, the characteristic mass is M_{500} while for the right-hand panels, the characteristic mass is M_{2500}

a function of its mass. We plot the median value of θ_E measured over the 50 lines of sight for an individual cluster; the error bars, denoting the 16th and 84th percentiles, reflect a measure of spread associated to the line-of-sight variance. We note that one of the clusters has a unusually large scatter in θ_E associated with the different orientations. This cluster has a small Einstein radius and is probably on a similar scale to angular resolution. The cluster mass is measured at two different overdensities: $\Delta = 500$ and $\Delta = 2500$. The Einstein radius increases with cluster mass, as expected, but the correlation is tighter at higher overdensities. This is in line with the expectation that high overdensities are responsible for strong lensing. The Einstein radius for a fixed value of M_{500} is slightly larger for clusters in the CSF simulations due to the higher concentration of these clusters. The asphericity, reflected in the size of the error bars, is also smaller for clusters in these simulations.

4.3 Unrelaxed Clusters

Unrelaxed clusters produce highly complex caustic structures which are the consequence of high mass subhaloes that lie within the field of view. These can create non-trivial complications in measurements of both the giant arc cross-section as well as the Einstein radius. In the previous sections we have discussed the lensing properties of relaxed clusters so as not to be susceptible to the effects of massive substructures. We now consider the subsample of unrelaxed clusters to verify how their properties differ and how they would affect lensing predictions. We remind the reader that at $z_L = 0.25$ there are 25 unrelaxed clusters and at $z_L = 0.5$ there are 20 unrelaxed clusters in our sample. Figure 14 shows the correlation between $\sigma_{7.5}$ and θ_E for clusters in the DM simulation comparing the relaxed and unrelaxed subsample. The unrelaxed clusters in our sample would introduce a large scatter. We verify that, as the threshold for the unrelaxedness parameter s_{max} , is increased, the scatter increases in the relaxed sub-sample. This is primarily due to giant

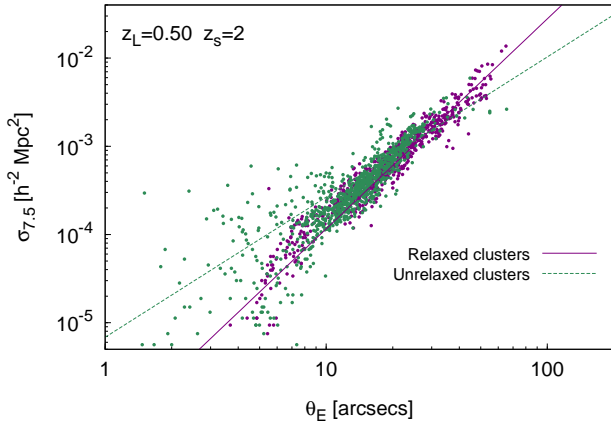


Figure 14. The relationship between the giant-arc cross section, $\sigma_{7.5}$, and the Einstein radius, θ_E , for each of the 50 lines of sight analysed for each relaxed cluster in the DM simulation at $z_L = 0.5$, for a source redshift of $z_s = 2$. Results for relaxed clusters are shown in purple (solid line of best fit), while the unrelaxed clusters are shown in green (dotted line of best fit). The unrelaxed sub-sample exhibits a larger intrinsic scatter.

arcs associated with substructure which induce a positive bias on the calculation of $\sigma_{7.5}$. The Pearson correlation coefficient, r , for unrelaxed clusters in *all* simulations, ranges from 0.87 to 0.92 at $z_L = 0.25$ and ranges from 0.82 to 0.90 at $z_L = 0.5$.

The scatter above the $\sigma_{7.5}$ - θ_E lines of best fit is primarily because of substructures that are large enough to produce distinct caustics (see top row of Figure 10), which induce a positive bias on the cross-section; as long as the caustics associated with projected substructures are well separated from the primary caustic, the Einstein radius measurement is not affected. On the other hand, if substructure are projected near the clusters centre, their caustics merge and produce highly elongated, critical curves (see bottom row of Figure 10), which artificially increases both measurements of strong lensing efficiency. However, the Einstein radius is affected more than the cross-section, thus down-scattering results for unrelaxed clusters with respect to the $\sigma_{7.5}$ - θ_E lines of best fit obtained for relaxed clusters.

Figure 15 shows the cumulative probability distribution of Einstein radii for the unrelaxed sub-sample. Clusters identified as unrelaxed are more likely to be merging systems, in which the main lens has a significantly lower mass than the total mass within the system. Hence, we find that typical Einstein radii are only 50 – 70 per cent of the size of Einstein radii for the relaxed counterparts.

We may now consider whether the effect of baryons on strong lensing properties is similar for the relaxed and unrelaxed sub-samples. Gas cooling and star formation produce clusters with a higher mass concentration; unrelaxed clusters have more substructures, which are also more compact than their collisionless counterparts (see, for example, the substructures visible in the cluster shown in Figure 5). Therefore the unrelaxed clusters in the CSF simulations have larger primary caustics than their DM counterparts, but, compared to relaxed clusters, are *also* more likely to host secondary caustics that merge with the primary and boost the Einstein radius. Thus, the Einstein radii at $z_s = 2$ for clusters

in the CSF simulations are higher by ~ 20 per cent than for their collisionless counterparts. This boost increases to ~ 50 – 70 per cent when we measure the Einstein radii at lower source redshifts. This is significantly larger than the boost for relaxed clusters.

The introduction of AGN feedback once again reduces the strong lensing efficiency of unrelaxed clusters; the Einstein radii at $z_s = 2$ for unrelaxed clusters in the AGN simulations are only 5 per cent larger than those for their collisionless counterparts in the DM simulations. The difference in strong lensing efficiency is essentially the same for both relaxed and unrelaxed clusters. However, a mixed sample — with both relaxed and unrelaxed clusters — would have smaller Einstein radii on average, than a relaxed-only sample.

4.4 Cluster Mass Profiles

In the previous sections, we have seen that gas cooling, star formation and stellar and AGN feedback have varying and often counteracting effects on strong lensing efficiencies. Here, we look at the mass profiles of the cluster-haloes to trace the origin of the change in strong lensing properties. However, a detailed analysis of the mass profile fitting and the effect of baryons on the concentration-mass relation is beyond the scope of this paper.

Previous analyses of non-radiative simulations in the literature have found that the gas profiles exhibit cores (e.g. Rasia et al. 2004; Rudd et al. 2008). Figure 16 shows the spherically averaged differential density profile for the relaxed clusters in two of our simulations: CSF and AGN. The profiles are shown for different components: dark matter, dark matter and gas, dark matter and gas and stars. The shaded regions mark the cluster-to-cluster scatter, while the error-bars mark the error of the mean; the small size of the error bars reflect the consistency in the profiles across the clusters.

In keeping with previous analyses, we confirm that within $r \lesssim 0.1R_{\text{vir}}$ gas cooling and star formation steepen the total mass profile with respect to DM-only simulations. In both CSF and AGN simulations, the baryonic component is dominated by stars within $r \lesssim 0.1R_{\text{vir}}$; the gas component has a core and is distributed primarily beyond 10 per cent of the virial radius. The steepening of the inner profile is associated with the build-up of stellar mass; AGN heating regulates star formation and therefore reduces the inner slope. We have mentioned earlier that comparisons between these two simulations must be interpreted carefully given that in the AGN simulations SN wind-speeds are increased while simultaneously introducing AGN feedback. Interestingly, Duffy et al. (2010) have shown that in simulations without AGN feedback, the inner slope of the DM profile of clusters at $z = 0$ actually steepens slightly when the SN wind-speed is reduced, but the stellar fraction within $r < 0.05R_{\text{vir}}$ is increased significantly, which we might expect to lead to an overall increase in the inner slope of the total mass profile. They find that the introduction of AGN feedback reduces both the stellar fraction within $r < 0.05R_{\text{vir}}$ and the inner-slope of the DM profile. Our findings are in agreement with Duffy et al. (2010) as well as several previous studies (e.g. Gnedin et al. 2004; Puchwein et al. 2005; Mead et al. 2010; Martizzi et al. 2012), in which the simulated clusters

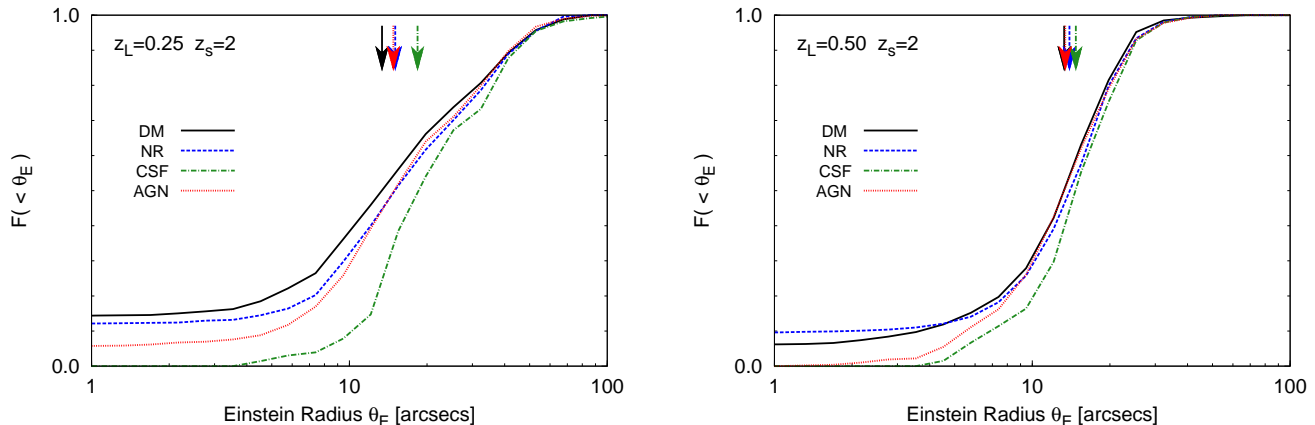


Figure 15. The probability distribution for Einstein radii combining 50 lines of sight through each of the unrelaxed clusters in the sample. The source redshift is $z_s = 2$. On the left panel, we show the results for clusters at $z_L = 0.25$; on the right panel, we show the results for clusters at redshift $z_L = 0.5$

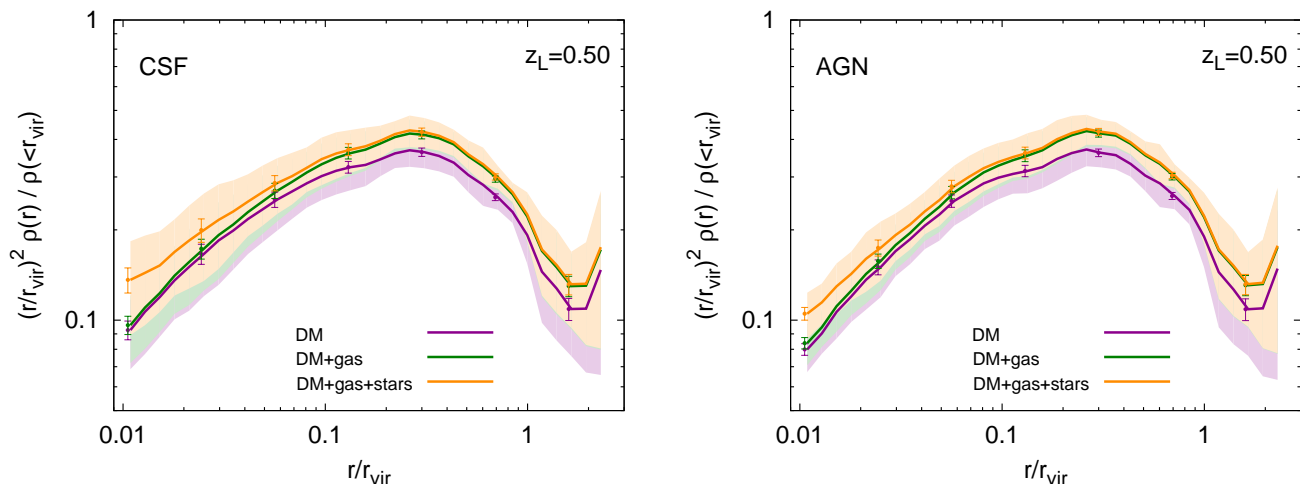


Figure 16. The differential density profile of dark matter (purple); dark matter and gas (green); dark matter, gas and stars (yellow). Clusters included in analysis are the relaxed sub-sample at $z_L = 0.5$ in the CSF simulation (left panel) and the AGN simulation (right panel). The solid lines represent the average over all clusters, the shaded regions (in the respective colours) are between the 16th and 84th percentiles among the clusters, while the error-bars correspond to the estimated error of the mean. The profile for each clusters has been normalised to the average mass density within the virial radius, and scaled with the square of the radius in order to reduce the dynamic range

are analysed at $z \lesssim 0.3$. We included in our analysis also clusters identified at higher redshift, $z = 0.5$, and found no strong redshift dependence of the results.

In order to see how the re-distribution of baryons affects the strong lensing, it is helpful to analyse the cumulative mass within different radii. In Figure 17 we show the cumulative mass profiles for the clusters at $z_L = 0.25$ and $z_L = 0.5$, respectively. The smallest radius shown corresponds to 1 per cent of the virial radius, which corresponds to $16 h^{-1}$ kpc for the smallest virial radius of all the clusters, or at least 3 times the softening length.

Our non-radiative NR simulations generate clusters with slightly more mass within $r < 0.1R_{\text{vir}}$ than their DM counterparts; however, this is too mild to produce significantly

stronger lenses, in agreement with the findings of Rozo et al. (2008) and Puchwein et al. (2005). The CSF simulations produce clusters that contain significantly more mass within $r < 0.1R_{\text{vir}}$ (see also Gnedin et al. 2004; Puchwein et al. 2005, for comparable results on steepening of density profiles in radiative simulations). However, these simulations suffer the ‘overcooling’ problem — on average, 22% of the baryonic mass within r_{500} in CSF clusters is in the form of stars — thus implying that the corresponding boost in strong lensing efficiency ought to be unrealistic. A more detailed comparison between simulation and observation results on the stellar fraction will be presented by Planelles et al. (2012, in prep).

AGN feedback reduces the total mass within $0.1 r_{\text{vir}}$ for

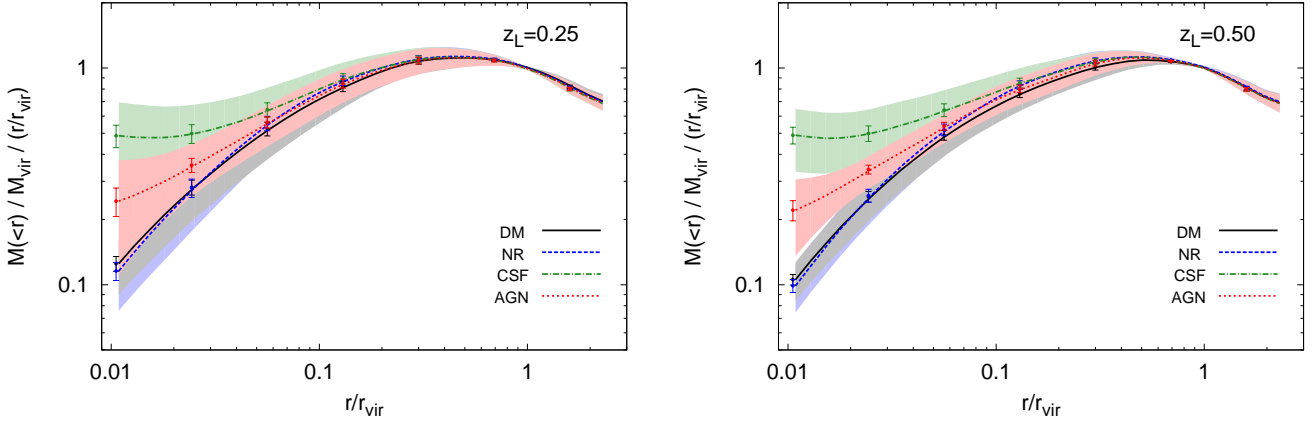


Figure 17. The cumulative mass profile for the relaxed clusters at $z_L = 0.25$ (left panel) and $z_L = 0.50$ (right panel). The lines reflect the average profile stacking all the clusters while the shaded regions are between the 16th and 84th percentiles among the clusters. The profile for each cluster has been normalised to the virial mass, and scaled with the radial distance in order to reduce the dynamic range

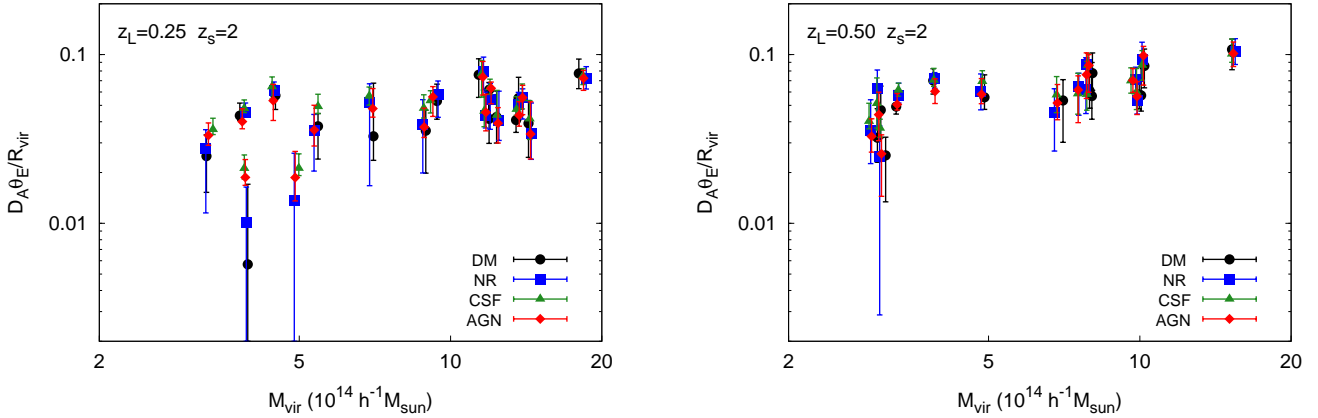


Figure 18. The Einstein radius relative to the cluster radius as a function of cluster mass. For each cluster, the median of the 50 analysed lines of sight are plotted with error bars reflecting the 16th and 84th percentiles over the distribution of lines of sight. On the left panel, we show relaxed clusters at $z_L = 0.25$, while relaxed clusters at $z_L = 0.50$ are on the right panel.

clusters at both redshifts¹. If we compare the DM and AGN simulations, we see that including AGN feedback results in clusters that contain more mass within $r < 0.03R_{\text{vir}}$ relative to their collision-less counterparts. However this does not translate into larger strong lensing efficiencies. The reason for this is seen in Figure 18 which shows the fraction of the virial radius encompassed by the Einstein radius at the cluster redshift, as a function of cluster mass. Typical Einstein radii are larger than the radius within which enclosed mass is affected by baryonic physics. So while clusters in the AGN simulations have a different structure with respect to their

DM counterparts, this difference does not produce stronger lenses, for sources at $z_s = 2$. If we consider the results for sources at $z_s = 1$, as shown in Table 1, the typical Einstein radii are smaller than for sources at $z_s = 2$. As a consequence, there is a higher significance to the probability that clusters in the CSF simulations are stronger lenses than their DM counterparts. Still, the strong lensing properties of clusters in the AGN simulations are still fairly consistent with the DM counterparts.

We defer a more detailed comparison with observations, extending the simulated cluster sample to a wider range of masses, to a future study. For the purpose of the present study, it is sufficient to say that the suppression of star formation due to gas heating by AGN feedback in the AGN simulations is responsible for the decrease in total mass in the cluster core, and subsequently, the decrease in the strong lensing efficiency of these clusters compared to their counterparts in the CSF simulations.

¹ It is informative to consider AGN feedback prescriptions implemented in Adaptive Mesh Refinement (AMR) codes, such as those presented by Teyssier et al. (2011). They report a stellar mass fraction of $f_* \approx 0.01$ which *increases with resolution* to $f_* \approx 0.02$. Although the concept of mass resolution is not directly comparable between SPH and AMR codes, their results do caution that AGN feedback may be sensitive to resolution.

5 CONCLUSIONS

In the present study, we have analysed the strong lensing efficiency of about 15 relaxed simulated clusters at $z_L = 0.25$ and $z_L = 0.5$. The clusters were re-simulated under a number of different physical models: dark matter only (DM); non-radiative gas (NR); cooling, star-formation, SN feedback (CSF); and additional AGN feedback (AGN). Our main findings are as follows.

- There are no significant differences in the strong lensing properties and density profiles of clusters modelled with dark matter only and those that include a non-radiative gas component.

- Gas cooling and star formation have the effect of increasing the giant arc counts and Einstein radii even in the presence of stellar feedback, which can push gas out of galaxies and reduce star formation.

- When AGN feedback is included in the simulations, the strong lensing efficiency of the clusters are significantly reduced. Einstein radii at $z_s = 2$ are only 5 per cent larger than those for the DM counterparts, a boost that is increased to 10–20 per cent for lower source redshifts. There is a smaller orientation dependence, reflecting a more spherical shape due to gas cooling, even in the presence of AGN feedback. Small Einstein radii ($\theta \lesssim 3''$) are less likely to be produced.

- The median Einstein radius is strongly correlated with the giant arc cross section for the relaxed cluster sub-sample. Unrelaxed clusters are especially problematic for the calculation of strong lensing efficiency using the production of giant lensing arcs as a proxy; they also have smaller strong lensing efficiencies.

- There exists a scaling relation between strong lensing efficiencies and mass, particularly for higher overdensities ($\Delta = 2500$). As we move to lower overdensities, the normalisation for the each simulation differs primarily due to the redistribution of baryons near the cluster core.

- We search for an explanation for these findings by analysing the mass profiles of our cluster sample; the distribution of mass in the centres of clusters are significantly influenced by baryonic physics. AGN feedback reduces the stellar mass in the core of otherwise ‘overcooled’ clusters. Nevertheless, within $r/R_{\text{vir}} \lesssim 0.03$ the total mass is still significantly larger than that of the DM counterparts. However, this does not translate to higher lensing efficiencies for $z_s = 2$, because $\theta_E \gtrsim 0.03R_{\text{vir}}$ for most clusters in our chosen mass range.

Where there is overlap in cluster masses and redshifts, our results are similar to those obtained by Duffy et al. (2010) and Mead et al. (2010) with regards to the effect of AGN feedback on density profiles and giant-arc cross-sections. The AGN feedback prescription used in each work are all inspired by the model of Springel et al. (2005) but with somewhat different implementations and choice of the relevant model parameters. Therefore, it is reassuring that the strong lensing predictions are not sensitive to these details. However Teyssier et al. (2011), who include mechanical AGN feedback associated with jets into an Eulerian AMR code, have noted that stellar fractions are sensitive to implementation. An open question is then whether different implementations of AGN feedback in different codes produce comparable effects on the inner density profiles of

massive halos and, therefore, on the strong lensing properties of galaxy clusters.

As for the comparison with observational data, available results on strong lensing arc statistics for samples of nearby and distant clusters have been recently carried out, for instance, by Horesh et al. (2010). Furthermore, the ongoing Cluster Lensing And Supernova survey with Hubble (CLASH; Postman et al. 2012) project, thanks to the superior sensitivity of deep HST imaging, is providing unprecedented detail in the internal mass distribution of galaxy clusters through strong lensing studies. These results represent an excellent test ground for the comparison with simulation results, like those presented in this paper. Self-consistent comparisons with data are deferred for future study, as this will require more careful selection of clusters, with a comparable mix of relaxed and unrelaxed objects in the observational and simulated samples, as well as consistent methods of measuring strong lensing properties. As Wyithe et al. (2001) have shown, a reduction in the lensing efficiency due to a decreased mass concentration may be partially compensated by a higher magnification for individual images. Therefore, a comparison of giant arc counts will require not only a prediction for the strong lensing cross-section, but also the magnification of images that are *potential* giant arcs, in order to determine if they would be detected in flux-limited imaging; this is particularly important for images that lie near the flux limit.

Approaches to resolving the arc statistics problem have generally involved questioning three aspects of the cosmological test: the assumed source redshift distribution, the realism of simulations, and the self-consistency in selection criteria for simulated and observed clusters. We prefer the Einstein radius as a proxy for strong lensing, since it allows one to avoid uncertainties with describing realistic source populations. None of the simulated models are tuned to reproduce *all* observable properties of clusters, but the AGN set of simulations is the most realistic one. Our study shows that AGN feedback is a game-changer; it’s hard to explain a possible discrepancy between observed and simulated lensing efficiency by resorting to the effect of baryons. Therefore, it will be crucial to make self-consistent comparisons between simulations and observations at a range of redshifts to understand if lensing efficiency truly presents a challenge for Λ CDM.

ACKNOWLEDGMENTS

The authors would like to thank Volker Springel for making available to us the non-public version of the GADGET-3 code, and Annalisa Bonafede for her help with generating the initial conditions for the simulations. The authors would also like to thank the anonymous referee for useful comments that improved the paper, as well as Weiguang Cui, Geraint Lewis, Giuseppe Murante, Susana Planelles, Ewald Puchwein, Joop Schaye, Piero Rosati and Simon White for helpful discussions. Simulations have been carried out at the CINECA supercomputing Centre in Bologna (Italy), with CPU time assigned through ISCR proposals and through an agreement with University of Trieste. MK acknowledges a fellowship from the European Commission’s Framework Programme 7, through the Marie Curie Initial Training Net-

work CosmoComp (PITN-GA-2009-238356). DF acknowledges funding from the Centre of Excellence for Space Sciences and Technologies SPACE-SI, an operation partly financed by the European Union, European Regional Development Fund and Republic of Slovenia, Ministry of Higher Education, Science and Technology. This work has been supported by the PRIN-INAF09 project “Towards an Italian Network for Computational Cosmology”, by the PRIN-MIUR09 “Tracing the growth of structures in the Universe” and by the PD51 INFN grant.

REFERENCES

- Barkana, R. Loeb, A. 2010, MNRAS, 405, 1969
- Bartelmann, M., Huss, A., Colberg, J. M., Jenkins, A., Pearce, F. R. 1998, A&A, 330, 1
- Blumenthal, G. R., Faber, S. M., Flores, R., Primack, J. R. 1986, ApJ, 301, 27
- Bonafede, A., Dolag, K., Stasyszyn, F., Murante, G., Borgani, S. 2011, MNRAS, 418, 2234
- Broadhurst, T. J. Barkana, R. 2008, MNRAS, 390, 1647
- Bryan, G. L. Norman, M. L. 1998, ApJ, 495, 80
- Bryan, S. E., Kay, S. T., Duffy, A. R., Schaye, J., Dalla Vecchia, C., Booth, C. M. 2012, ArXiv e-prints
- Chabrier, G. 2003, PASP, 115, 763
- Crone, M. M., Evrard, A. E., Richstone, D. O. 1996, ApJ, 467, 489
- Cui, W., Borgani, S., Dolag, K., Murante, G., Tornatore, L. 2012, MNRAS, 2981
- Dalal, N., Holder, G., Hennawi, J. F. 2004, ApJ, 609, 50
- D’Onghia, E. Navarro, J. F. 2007, MNRAS, 380, L58
- Duffy, A. R., Schaye, J., Kay, S. T., Dalla Vecchia, C. 2008, MNRAS, 390, L64
- Duffy, A. R., Schaye, J., Kay, S. T., Dalla Vecchia, C., Battye, R. A., Booth, C. M. 2010, MNRAS, 405, 2161
- Efstathiou, G., Sutherland, W. J., Maddox, S. J. 1990, Nat, 348, 705
- Fabjan, D., Borgani, S., Tornatore, L., Saro, A., Murante, G., Dolag, K. 2010, MNRAS, 401, 1670
- Ferland, G. J., Korista, K. T., Verner, D. A., Ferguson, J. W., Kingdon, J. B., Verner, E. M. 1998, PASP, 110, 761
- Gnedin, O. Y., Kravtsov, A. V., Klypin, A. A., Nagai, D. 2004, ApJ, 616, 16
- Haardt, F. Madau, P. 2001, in Clusters of Galaxies and the High Redshift Universe Observed in X-rays, ed. D. M. Neumann J. T. V. Tran
- Hattori, M., Watanabe, K., Yamashita, K. 1997, A&A, 319, 764
- Horesh, A., Maoz, D., Ebeling, H., Seidel, G., Bartelmann, M. 2010, MNRAS, 406, 1318
- Horesh, A., Maoz, D., Hilbert, S., Bartelmann, M. 2011, MNRAS, 418, 54
- Kazantzidis, S., Kravtsov, A. V., Zentner, A. R., Allgood, B., Nagai, D., Moore, B. 2004, ApJ Lett., 611, L73
- Komatsu, E., et al. 2011, ApJS, 192, 18
- Kravtsov, A. Borgani, S. 2012, ArXiv e-prints
- Lewis, G. F., Babul, A., Katz, N., Quinn, T., Hernquist, L., Weinberg, D. H. 2000, ApJ, 536, 623
- Li, G.-L., Mao, S., Jing, Y. P., Bartelmann, M., Kang, X., Meneghetti, M. 2005, ApJ, 635, 795
- Macciò, A. V., Dutton, A. A., van den Bosch, F. C. 2008, MNRAS, 391, 1940
- Martizzi, D., Teyssier, R., Moore, B., Wentz, T. 2012, MNRAS, 422, 3081
- McCarthy, I. G., et al. 2010, MNRAS, 406, 822
- Mead, J. M. G., King, L. J., Sijacki, D., Leonard, A., Puchwein, E., McCarthy, I. G. 2010, MNRAS, 406, 434
- Meneghetti, M., Bolzonella, M., Bartelmann, M., Moscardini, L., Tormen, G. 2000, MNRAS, 314, 338
- Meneghetti, M., Fedeli, C., Zitrin, A., Bartelmann, M., Broadhurst, T., Gottlöber, S., Moscardini, L., Yepes, G. 2011, A&A, 530, A17+
- Meneghetti, M., Jain, B., Bartelmann, M., Dolag, K. 2005, MNRAS, 362, 1301
- Navarro, J. F., Frenk, C. S., White, S. D. M. 1996, ApJ, 462, 563
- Neto, A. F., et al. 2007, MNRAS, 381, 1450
- Oguri, M. 2004, PhD thesis, The University of Tokyo
- Padovani, P. Matteucci, F. 1993, ApJ, 416, 26
- Postman, M., et al. 2012, ApJS, 199, 25
- Power, C., Knebe, A., Knollmann, S. R. 2011, MNRAS, 1734
- Prada, F., Klypin, A. A., Cuesta, A. J., Betancort-Rijo, J. E., Primack, J. 2012, MNRAS, 423, 3018
- Puchwein, E., Bartelmann, M., Dolag, K., Meneghetti, M. 2005, A&A, 442, 405
- Puchwein, E. Hilbert, S. 2009, MNRAS, 398, 1298
- Puchwein, E., Sijacki, D., Springel, V. 2008, ApJ Lett., 687, L53
- Rasia, E., Tormen, G., Moscardini, L. 2004, MNRAS, 351, 237
- Redlich, M., Bartelmann, M., Waizmann, J.-C., Fedeli, C. 2012, ArXiv e-prints
- Rozo, E., Nagai, D., Keeton, C., Kravtsov, A. 2008, ApJ, 687, 22
- Rudd, D. H., Zentner, A. R., Kravtsov, A. V. 2008, ApJ, 672, 19
- Sadeh, S. Rephaeli, Y. 2008, MNRAS, 388, 1759
- Schneider, P., Ehlers, J., Falco, E. E. 1992, Gravitational Lenses (Springer-Verlag Berlin Heidelberg New York. Also Astronomy and Astrophysics Library)
- Sijacki, D., Springel, V., Di Matteo, T., Hernquist, L. 2007, MNRAS, 380, 877
- Springel, V. 2005, MNRAS, 364, 1105
- Springel, V., Di Matteo, T., Hernquist, L. 2005, MNRAS, 361, 776
- Springel, V. Hernquist, L. 2003, MNRAS, 339, 289
- Teyssier, R., Moore, B., Martizzi, D., Dubois, Y., Mayer, L. 2011, MNRAS, 414, 195
- Thomas, P. A., et al. 1998, MNRAS, 296, 1061
- Tormen, G., Bouchet, F. R., White, S. D. M. 1997, MNRAS, 286, 865
- Tornatore, L., Borgani, S., Dolag, K., Matteucci, F. 2007, MNRAS, 382, 1050
- van de Voort, F., Schaye, J., Booth, C. M., Dalla Vecchia, C. 2011, MNRAS, 415, 2782
- White, S. D. M. Frenk, C. S. 1991, ApJ, 379, 52
- Wiersma, R. P. C., Schaye, J., Smith, B. D. 2009, MNRAS, 393, 99
- Wyithe, J. S. B., Turner, E. L., Spergel, D. N. 2001, ApJ, 555, 504

Zitrin, A., Broadhurst, T., Barkana, R., Rephaeli, Y.,
Benítez, N. 2011, MNRAS, 410, 1939

This paper has been typeset from a \TeX / \LaTeX file prepared
by the author.